ULTRAFAST LEED OF BISMUTH ON SILICON (001)

A thesis

submitted to

Indian Institute of Science Education and Research, Pune for the partial fulfillment of the requirements for the BS-MS dual degree

by

Nandana V Uday

20201145

Indian Institute of Science Education and Research, Pune

Dr. Homi Bhabha Road, Pashan, Pune 411008, India.

April 2025

Supervisor: Prof. Dr. Claus Ropers

Max Planck Institute of Multidisciplinary Sciences, Göttingen, Germany

Certificate

This is to certify that this dissertation entitled “Ultrafast LEED of Bismuth on Silicon (001)” towards the partial fulfillment of the BS-MS dual degree programme at the Indian Institute of Science Education and Research, Pune, represents study/work carried out by Nandana V Uday at Max Planck Institute of Multidisciplinary Sciences, under the supervision of Prof. Dr. Claus Ropers during the academic year 2024-2025.

Supervisor: Prof. Dr. Claus Ropers
Max Planck Institute of Multidisciplinary Sciences
Göttingen, Germany

Sign: 

Expert: Prof. Dr. Pankaj Mandal
Indian Institute of Science Education and Research(IISER)
Pune, India

This thesis is dedicated to my family and friends.

Declaration

I hereby declare that the matter embodied in the report entitled " Ultrafast LEED of Bismuth on Silicon (001)" are the results of the work carried out by me at the Department of Ultrafast Dynamics, Max Planck Institute of Multidisciplinary Sciences, under the supervision of Prof. Dr. Claus Ropers and the same has not been submitted elsewhere for any other degree. Wherever others contribute, every effort is made to indicate this clearly, with due reference to the literature and acknowledgment of collaborative research and discussions.

Nandana V Uday

20201145

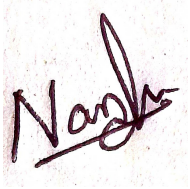

Acknowledgements

First and foremost, I would like to express my sincere gratitude to my supervisor, Prof. Dr. Claus Ropers, for his invaluable guidance, support, and motivation throughout this work. His valuable feedback and extensive expertise have been key contributors to the successful completion of my thesis.

I would like to thank all ULEED members - Felix Kurtz, Alp Akbıyık, Dr. Hannes Boeckmann, Dr. Dennis Epp, Florian, and Frank- for all the fruitful discussions and support. I have gained a great deal of knowledge and experience during this time from all these people. The time and effort Felix, Alp, and Hannes dedicated to helping me learn the experiment, conduct analysis, and gain overall research experience deserve special thanks.

I would like to express my deep gratitude to Prof. Dr. Pankaj Mandal for agreeing to be my expert member. Working in his lab is what fueled my interest in the ultrafast field.

Lastly, I would like to express my gratitude to my family and friends. My parents, without whose support, none of this would have been possible. Their firm belief in me has been my greatest source of strength and motivation. Thanks to Riteeka Tanwar, whose research ethics and sincerity have always guided me. My friends, who supported me through all these years and always made time for each other, are the greatest blessing. Special thanks to Avanthika, Utthara, Lakshmi, Malu, KS, and Unni for being my constant support. Weekly video chats with Avanthika, Abhay, Akshay, Bhageerath and Viju has always been the fun and energy past year.

Contents

List of Figures

List of Tables

Abstract

Ultrafast dynamics of epitaxial bismuth films on Si(001) substrate when exposed to femtosecond laser pulses is investigated using Ultrafast Low Energy Electron Diffraction (ULEED). Owing to its high temporal resolution and surface sensitivity, ULEED is a powerful tool for probing ultrathin films and interfaces.

Upon laser excitation of the bismuth film, a non-equilibrium electronic system is created, subsequently transferring energy to the lattice through electron-phonon coupling, causing a rapid rise in the surface temperature. Following this, the heat transfer by phonons through the thin film-substrate interface is monitored to extract cooling times from the transient lattice temperature of the bismuth film. The interface between two materials in a heterostructure serves as a barrier to the diffusive transfer of thermal energy, thereby hindering heat flow across the boundary. To quantify these processes, the rise time and cooling time constant are systematically analyzed, with a focus on their dependence on laser fluence and film thickness.

Recently, it was shown that the thermal transport from Bi(111) films into a Si(001) substrate is reduced when films are thinner than the phonon mean free path due to total internal reflection where phonon propagation becomes complex. To study the non-equilibrium phonon dynamics in this process, ULEED is a suitable and direct means of providing ultrafast temporal and high-momentum resolution. By analyzing the momentum-resolved map of a transient inelastic scattering background, we aim to identify phonon trapping, depopulation, and thermalization.

1 Introduction

1.1 Low Energy Electron Diffraction

According to quantum mechanics, a particle exhibits diffraction when the de Broglie wavelength of the wave is comparable to the lattice constant of a crystal ($\frac{h}{p} \leq a$). This theory was experimentally proven for electrons in an accidental discovery by Davisson and Germer while studying the scattering of electrons from a polycrystalline nickel sample. For low-energy electrons, the de Broglie wavelength is comparable to the lattice spacing; for instance, an electron with an energy of 100 eV has a wavelength of approximately 3.87 Å, matching typical interatomic spacings in crystals.

Low-energy electrons have a higher chance of undergoing inelastic scattering processes, which leads to rapid energy loss. This consequently results in a shorter inelastic mean free path or smaller penetration depths of less than a few angstroms, represented in a universal scaling curve (see Figure 1a). When the electron energy is in a range between 10 to 100 eV, the inelastic mean free path is minimal. Consequently, the electrons can only penetrate into the upper layers, resulting in higher surface sensitivity. Thus, Low Energy Electron Diffraction (LEED) is one of the most prominent techniques to study the periodicity and arrangement of surfaces.

The basic components of a LEED setup are an electron gun, ultrahigh vacuum, fluorescent detector, and a clean sample surface (see Figure 1b). An electron gun has a cathode filament, generally made of tungsten. It produces a continuous beam of electrons when heated. When a negative potential relative to the sample is applied, this beam accelerates and is then further collimated by electrodes or electron lenses. This beam strikes the sample and is elastically backscattered. A fluorescent screen is used to detect these electrons in which a diffraction pattern is formed.

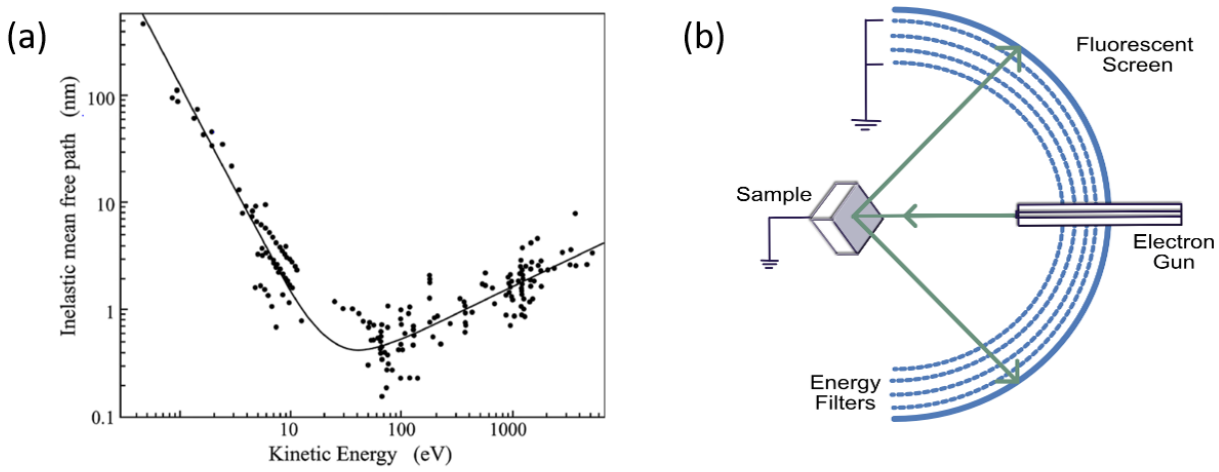

Figure 1: (a) Universal scaling curve for the electron mean free path. Adapted from [1]. (b) Basic setup of LEED.

1.2 Kinematic Diffraction theory

Kinematic LEED theory is the most basic theoretical approximation for surface structure analysis of LEED patterns. The theory puts forward the 'kinematic limit of diffraction' in which an electron that is elastically scattered once due to the electrostatic potential of an atom is not scattered again by another surface atom. When high-energy electrons are incident on an atom, the interatomic potential V(r) is relatively weak. This allows for using Born's approximation to calculate the amplitude of scattered beams. However, it is ineffective in the case of low-energy electrons since multiple scattering processes are difficult to avoid. But single scattering theory is sufficiently accurate for studying LEED patterns.

The theory considers a plane wave as the incident, monochromatic electron beam [2]:

$$A_i = A_0 exp(i\vec{k_o}.\vec{r}) \tag{1}$$

where A_i is the amplitude of incident wave, A_o is a constant, $\vec{k_o}$ is the incident wave vector, and $\vec{r}$ is a space vector.

The amplitude of the scattered beam after diffraction is given by:

$$A_s = A_0 \left[\Sigma_n \alpha f_n(\vec{s}) exp(-i\vec{s}.\vec{r_n}) exp(i\vec{k}_{out}.\vec{r}) \right] \tag{2}$$

where $f_n(\vec{s})$ is the atomic scattering factor for the nth atom located at a position $r_n, \vec{s} = \vec{k}_{out} - \vec{k}_0$ is the momentum transfer, and $\vec{k}_{out}$ is the wave vector of the scattered wave.
The emergence of diffraction peaks is subject to two requirements. Kinematic diffraction states that the scattering is elastic and hence energy conservation between the incoming and scattered beam results in:

$$E = \frac{\hbar^2}{2m} |\vec{k_o}|^2 = \frac{\hbar^2}{2m} |\vec{k_{out}}|^2 \tag{3}$$

The next requirement is regarding the Bragg conditions. For that, we consider a structure factor $S = \sum_n f_n exp(i\vec{s} \cdot \vec{r_n})$. which controls the diffracted pattern.

Let the atomic position $\vec{r_n}$ for a two-dimensional surface be denoted by $\vec{r_n} = \vec{R_p} + m_1\vec{a_1} + m_2\vec{a_2}$ where $\vec{a_i}$ are the basis vectors of the lattice, m_i are integers and $\vec{R_p}$ are the positions of the atoms within one unit cell. For surface characterizations, the normal coordinate of the diffracting lattice is omitted, hence the two-dimensional surface structure is:

$$S^{(2)} = \left[\Sigma_p f_p exp(i\vec{s}_{||}.\vec{R_p}) \right] \left[\Sigma_{\vec{m_1},\vec{m_2}} exp(i\vec{s}_{||}.(\vec{m}_1\vec{a}_1 + \vec{m}_2\vec{a}_2)) \right] \tag{4}$$

For bulk diffraction (3D crystals), we use the full scattering vector $\vec{s}$. However, for LEED, which studies surfaces, we focus on the parallel component $\vec{s}_{||}$, which is the projection of $\vec{s}_{||}$ onto the surface plane since a 2D lattice lacks periodicity in the direction normal to the surface. This second sum results in a Dirac delta function, meaning that diffraction occurs only at specific points in reciprocal space. That is, the sum over the two-dimensional vectors is proportional to $\delta(\vec{s}_{||} - g^{(2)})$ where $\vec{s}_{||}$ is the component of s parallel to the surface and $g^{(2)}$ is any of the two-dimensional reciprocal lattice vectors of the surface lattice. This enforces that diffraction occurs only when $\vec{s}_{||}$ matches a two-dimensional reciprocal lattice vector $g^{(2)}$.

The Bragg conditions for diffraction for LEED are:

$$\vec{s}_{||} = \vec{k}_{out,||} - \vec{k}_{o,||} = \vec{g}^{(2)} = \vec{g} \tag{5}$$

The stated conditions impose no restrictions to the momentum transfer perpendicular to the surface, but the momentum transfer parallel to the surface must match the reciprocal lattice vector of the surface lattice. These conditions are best represented by the Ewald sphere.

1.3 Ewald Sphere

The Ewald sphere is a simple geometric construction in reciprocal space which represents a set of conditions in which diffraction occurs. A sphere is drawn with the center at the origin of the incident wave vector $\vec{k}_0$ with radius $|\vec{k}_0| = k$. Laue condition states that diffraction happens when $\vec{k}_{out} - \vec{k}_0$ is a reciprocal lattice vector where $\vec{k}_{out}$ is a Bragg-reflected wave. A reflection takes place only when a reciprocal lattice point intersects the Ewald sphere (see Figure 2).

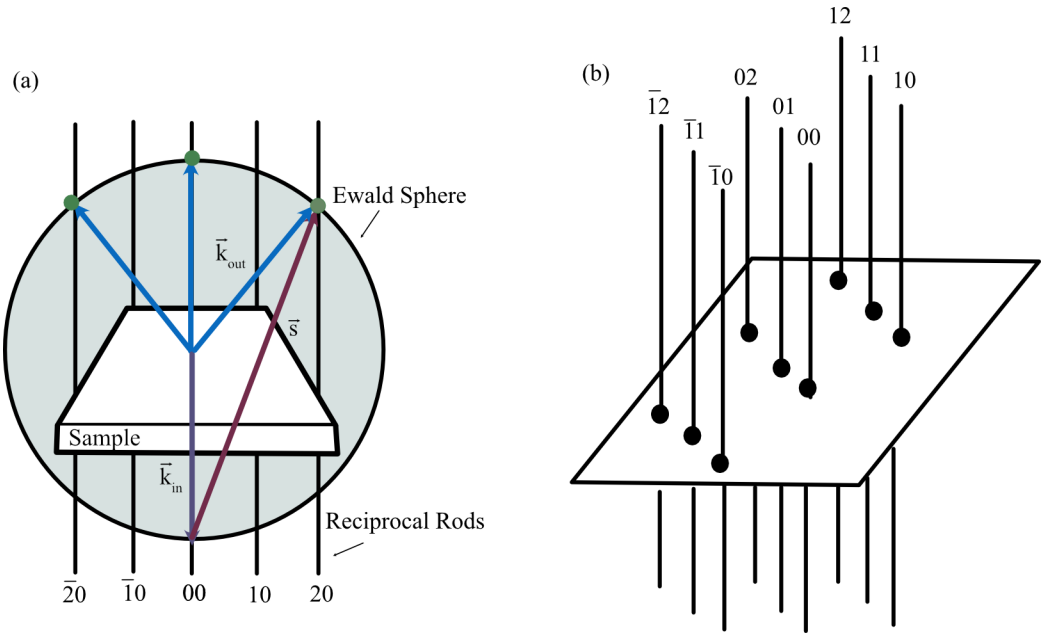

Figure 2: (a) 2D representation of the Ewald sphere.Incident wave vector $\vec{k}_0$ parallel to reciprocal rods is shown. Reflection happens only when a reciprocal lattice point intersects the Ewald sphere. (b) Reciprocal space of a 2D lattice. Adapted from [3].

However, in the study of diffraction from surfaces, the bulk 3D model is replaced by a 2D model. Here, reciprocal lattice points are substituted with reciprocal lattice rods that are oriented perpendicular to the surface. Also, $s = \vec{k}_{out} - \vec{k}_0$ be a vector connecting any two points on the rods. At the point of intersection between rods and sphere, momentum conservation and Bragg conditions are fulfilled.

1.4 Debye Waller Effect

Up to now, atoms were considered to be static. However, taking into account thermal fluctuations, atomic positions become $\vec{r}_n(t) = \vec{r}_{n,0} + \vec{u}_n(t))$ where $\vec{u}_n(t))$ is the time-dependent displacement [4] and $\vec{r}_{n,0}$ is the equilibrium (average) position of the atom. Since intensity is the squared amplitude of the scattered wave, from equation (2) we get:

$$I(t) = |\sum_n f(s)\exp(-i\vec{s}.\vec{r}_n(t))|^2 \tag{6}$$

Substituting the atomic position expression:

$$I(t) = f^2(s)\sum_{n.m}\exp(i\vec{s}.(\vec{r}_{n,0} - \vec{r}_{m,0}))\exp(i\vec{s}.(\vec{u}_n(t) - \vec{u}_m(t))) \tag{7}$$

Taking the time average, we get:

$$< I(t) >= f^2(s)\sum_{n.m}\exp(i\vec{s}.(\vec{r_{n,0}} - \vec{r_{m,0}})) < \exp(i\vec{s}.(\vec{u}_n(t) - \vec{u}_m(t))) > \tag{8}$$

If $\vec{s}.\vec{u}_n(t) = u_{sn}$

$$< I(t) >= f^2(s)\sum_{n.m}\exp(i.\vec{s}.(\vec{r_{n,0}} - \vec{r_{m,0}})) < \exp(i\vec{s}.(u_{sn} - u_{sm})) > \tag{9}$$

Under small atomic displacements,

$$\exp(isx) \simeq 1 + isx - \frac{1}{2}(sx)^2 + i\frac{1}{6}(sx)^3 \tag{10}$$

Taking the average of the fluctuating displacement:

$$< \exp(isx) > \simeq 1 - \frac{1}{2} < (sx)^2 > + ... \simeq \exp\left(-s^2 < x >^2\right)/2 \tag{11}$$

This means that the diffraction intensity is modified as:

$$< I(t) >= f^2(s) \sum_{n.m} \exp\left(-\frac{s^2}{2} < (u_n - u_m)^2 > \right) \exp(i\vec{s}.(\vec{r}_{n,o} - \vec{r}_{m,o})) \tag{12}$$

$$< I(t) >= f^2(s) \sum_{n.m} \exp\left(-\frac{(su_n)^2}{2} \right) \exp\left(-\frac{(su_m)^2}{2} \right) \exp\left(-s^2 < (u_n u_m) >\right) \exp(i\vec{s}.(\vec{r}_{n,o} - \vec{r}_{m,o})) \tag{13}$$

$$< I(t) >= f^2(s) \sum_{n.m} \exp\left(-\frac{(su_n)^2}{2} \right) \exp\left(-\frac{(su_m)^2}{2} \right) (1 - s^2 < (u_n u_m) >) + ..) \exp(i\vec{s}.(\vec{r}_{n,o} - \vec{r}_{m,o})) \tag{14}$$

Then the first-order contribution to the intensity of the diffraction pattern is

$$I(t) = I_0 \exp(-2M) \tag{15}$$

where we define the Debye-Waller factor (DWF) as:

$$\exp(-2M) = \exp\left(-s^2 < u^2 >\right) \tag{16}$$

For the Debye model at elevated temperatures, it can be expressed as:

$$\exp(-2M) = \exp\left(-s^2 < u^2 >\right) = \exp\left(\frac{-3\hbar^2 |\vec{s}|^2 T}{m_a k_b {\Theta_D}^2} \right) \tag{17}$$

Due to collective lattice vibrations, a reduction in intensity is observed at scattering vector q. Fluctuating atomic positions lead to a partial cancellation of the scattered waves leading to reduced intensity. This effect becomes more pronounced at higher temperatures as atomic vibrations become more pronounced.

1.5 Diffuse Scattering Theory

When electrons interact with a material, it is either elastically or inelastically scattered. Inelastically scattered electrons contribute to the diffuse background. Applying first-order perturbation theory, total scattering intensity at scattering vector q is reduced to first-order scattering theory [5, 6];

$$I_1(Q) = \Sigma_\nu \frac{\hbar}{2\omega_{q\nu}}(2n_{q\nu}+1)|F_{q\nu}(Q)|^2 \tag{18}$$

where $n_{q\nu}$, $\omega_{q\nu}$ $F_\nu(Q)$ are population, frequency, and structure factor of the phonon mode ν with the wave vector q where q = Q−G, in which G is the reciprocal lattice vector nearest to Q.

The contribution of each phonon mode on intensity is given by the one phonon structure factor.

$$F_{q\nu}(Q) = \Sigma_K f_K(Q)\frac{e^{-W_K(Q)}}{\sqrt{M_K}}|Q.e_{q\nu}|^2 \tag{19}$$

The diffuse background intensity is influenced by the contribution of each phonon mode which is :

$$\omega_{q\nu} = \frac{\frac{1}{\omega_{q\nu}}(2n_{q\nu}+1)|F_{q\nu}|^2}{\Sigma_{q_\perp\nu}\frac{1}{\omega_{q\nu}}(2n_{q\nu}+1)|F_{q\nu}|^2} \tag{20}$$

This equation tells that phonons with lower frequencies contribute more to the diffuse intensity or higher temperature leads to more diffuse scattering as the phonon population increases.

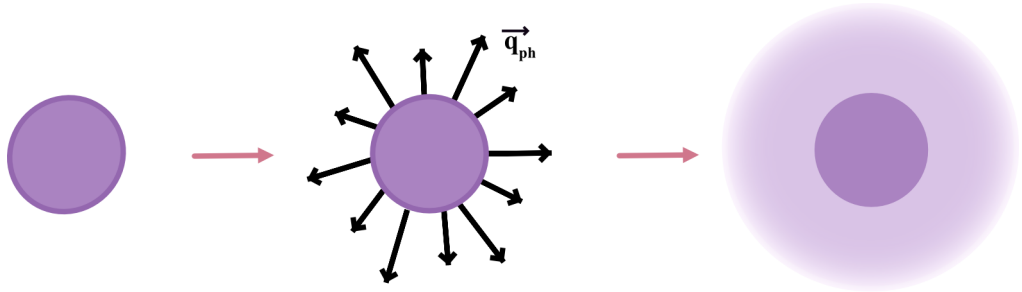

Figure 3: Schematic illustration of Diffuse Scattering.

1.6 Phonon Transport

When a phonon that travels from medium A to medium B reaches the interface, there are two possibilities if the velocity of phonons in medium B is higher than medium A. Phonons that are incident at an angle greater than a critical angle are totally reflected back to medium A. All the other phonons that are incident at an angle less than this critical angle are transmitted to medium B. Hence, there is a critical cone in which all the phonons inside it are transmitted and not reflected back [7].

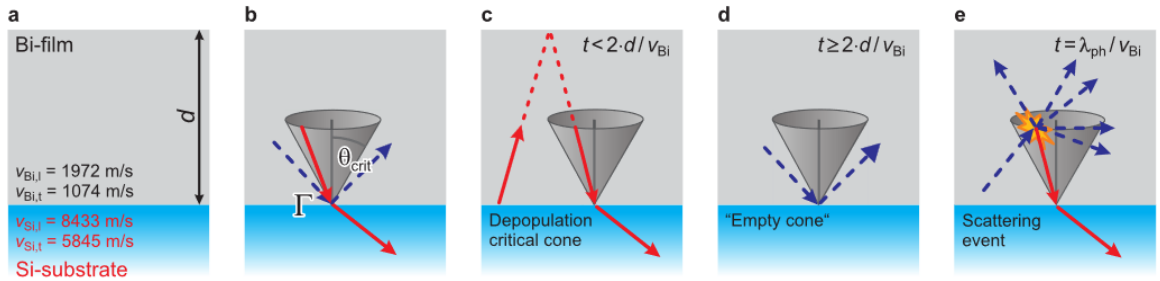

Figure 4: Model depicting the phonon dynamics of ultrathin bismuth film on Si(001).Taken from [8].

For example, in ultrathin bismuth films on silicon(001), velocity of phonons in silicon being higher in bismuth ($v_{Si,l}$ = 8433 m/s, $v_{Si,t}$ = 5845 m/s, $v_{Bi,l}$ = 1972 m/s, $v_{Bi,t}$ = 1074 m/s), phonons are reflected back if the angle of incidence greater than $\arcsin(\frac{v_{Bi}}{v_{Si}})$. The film stops cooling after all the phonons inside the critical cone are transmitted to the substrate. The critical cone must be repopulated by phonon scattering if cooling has to continue. For thicker films, since transit time is longer than the scattering time, there is enough time for the phonons to repopulate and continue the cooling. However, for films thinner than half of the mean free path of phonons, phonons escape too quickly, leading to a longer time for cooling (see Figure 4) [8].

Hanisch-Blicharski et al. argue that the ballistic transport of phonons facilitates heat transport and not diffusive transport due to the absence of sources of diffusive scattering in bismuth

films on silicon(001). In contrast, heat transport across bismuth film on silicon(111) is by diffusive phonon scattering due to the complex reconstruction of Si(111).

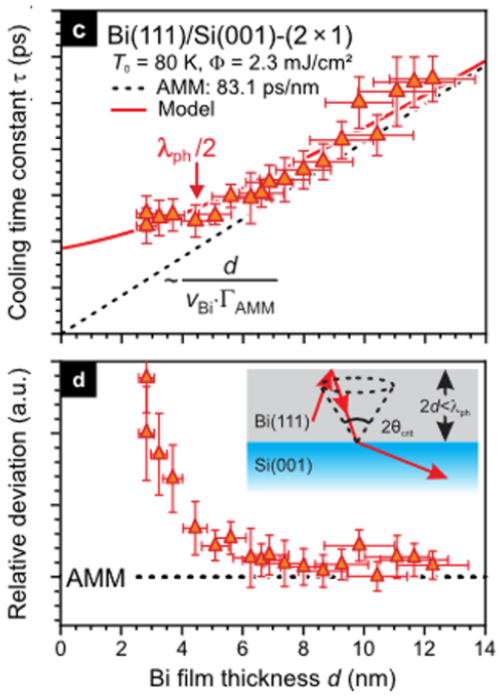

Figure 5: Cooling Time constant for different thicknesses of bismuth films on Si(001). Taken from [8].

2 Experimental Methods and Materials

2.1 ULEED

Ultrafast Low Energy Electron Diffraction (ULEED) is a potent tool for investigating surface structure dynamics in the time domain [9]. In this technique, an optical pump pulse excites the sample, and an electron probe pulse, which arrives after a varying time delay Δt, is used to obtain the time-resolved information (see Figure 6). In this setup, the electron pulse is photoemitted from a tungsten nanotip using pulsed UV light.

The laser system consists of a pulsed femtosecond Yb:YAG laser amplifier system (Pharos, Light conversion) with a central wavelength of λ_c = 1030 nm, pulse duration of $\Delta\tau$ = 200 fs, pulse energy of E_p = 150 μJ, output power of P_{out} = 15 W and a repetition rate of f_{rep} = 100 KHz. It includes a regenerative amplifier seeded by an internal oscillator and pumps an optical parametric amplifier (OPA, Orpheus) and a non-collinear optical parametric amplifier (NOPA, Orpheus -N). The fundamental frequency or the frequency-converted output of the OPA (signal and idler wavelengths are tunable between 630 to 1030 nm and 1030 to 2600 nm, respectively) is used to excite the sample, whereas the NOPA output (tunable between 650 to 900 nm) is employed to produce pulses of second harmonic wavelength of 400 nm. These 400 nm pulses are characterized by an ultrashort duration of approximately 40 fs and an energy of 100 nJ per pulse.

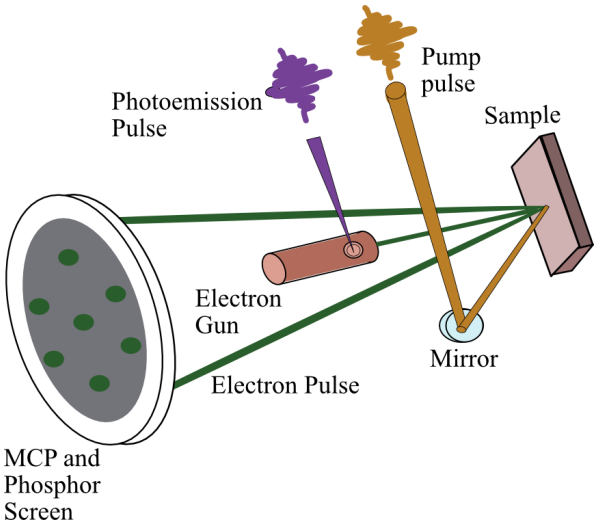

Figure 6: Basic Concept of ULEED. Optically excited sample is probed with electron pulses and detected using a microchannel plate.

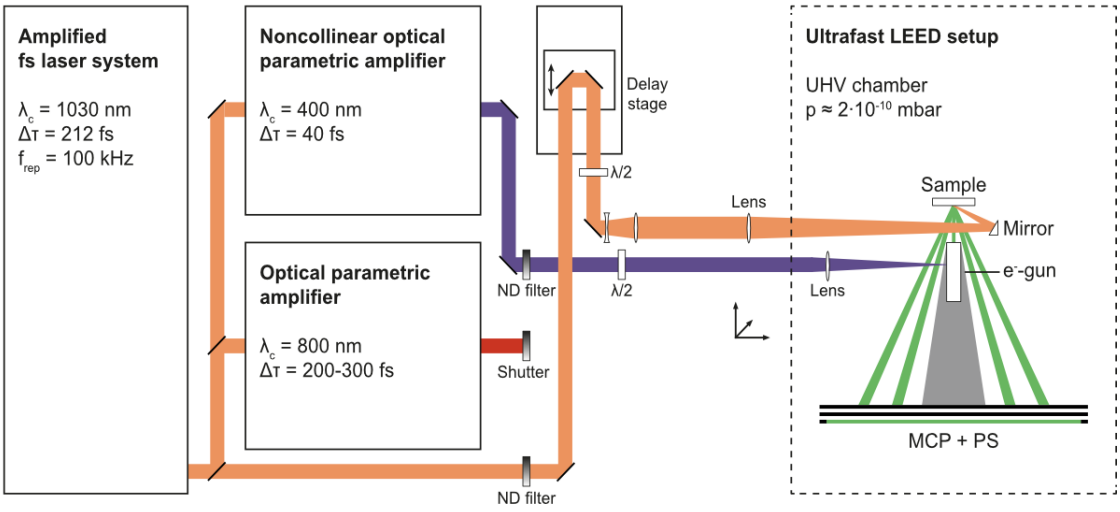

Figure 7: Schematic drawing of ULEED setup (Adapted from [10]).

The 400 nm beam is attenuated using a set of neutral density filters and passes through a $\lambda/2$ waveplate for matching its polarization with the nanotip orientation. Electron probe pulses are generated by focusing these 400 nm pulses onto a nanoscopic tungsten tip using an aspheric lens of focal length 22 mm, mounted on an XYZ piezo (attocube). The electron pulses are produced via Two-Photon PhotoEmission (2PPE). In the measurements, delay stages are used to vary the time delay between the pump and the probe pulses in order to obtain time-resolved dynamics (see Figure 7 and 8).

Apart from the electron gun, the UHV chamber houses a load lock with a sample storage, preparation chamber with a motorized LHe/LN_2 cryo-manipulator, Direct Current Heater (DCH), gas inlet, an argon ion sputtering source for sample cleaning, an electron beam evaporator with a quartz crystal microbalance, mass spectrometer and a measurement chamber with the electron guns and the detector. The detector is composed of microchannel plates (MCP) for amplification of electrons and a phosphorous screen. The number of backscattered electrons from the sample is very low (in the order of 1 to 10 per pulse), which necessitates the amplification of these electrons. Amplification happens when there is a secondary electron emission due to the collision of electrons with the walls of the microchannels. A

sCMOS (scientific complementary metal–oxide–semiconductor) camera is used to acquire the diffraction pattern.

Time-resolved spot profile analysis can be used to analyze the momentum resolution. To figure out the time resolution of the setup, when the laser hits the sample, diffraction patterns are recorded at different time delays to see how certain diffraction spots change in intensity. By fitting the intensity evolution with an error function—essentially a mathematical model that accounts for both the sample's fast response and the system's slower measurement limit—researchers can estimate how fast the experimental setup is able to track structural changes.

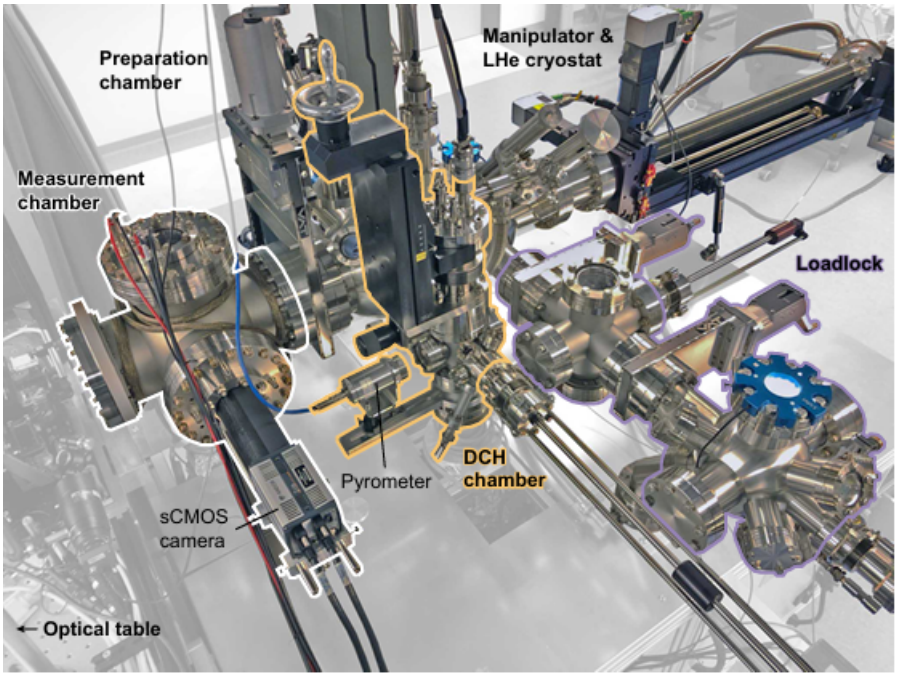

Figure 8: UHV setup of ULEED (taken from [10]).

2.2 Electron Source

Since the traditional surface diffraction techniques lack temporal resolution, designing an ultrafast pulsed electron source was the most important step in the development of ULEED. However, this was faced with many challenges, which include space-charge-induced broad-

ening due to the Coulomb repulsion between electrons, differences in emission angles and trajectories, finite energy width ΔE of the electron spectrum, etc. Gero Storeck and colleagues designed two electron sources based on ultrafast photoemission, where femtosecond laser pulses are directed onto a photocathode, triggering the photoelectric effect to produce electron pulses on the picosecond timescale.[11]. These sources rely on the lighting rod effect or the local electric field enhancement at the apex of a nanometric tip. Electrostatic fields strongly accelerate electron pulses within the static electric field of a biased tip while also amplifying the oscillating electric field of the incoming laser pulse. Regions with intensified electric fields correspond to areas of higher light intensity, leading to multi-photon electron emission as a result of nonlinear effects.

Most efforts in the further development of the setup aimed at an improved time resolution. As Coulomb repulsion and Dispersion are main sources of pulse broadening, a possible route lies in reducing the distance between the sample and gun. However, in this way, the gun increasingly shadows much of the backreflected LEED pattern. In order to mitigate this effect, a miniaturized electron source - namely milimeter and micrometer guns, were developed in the group.

The minigun yields a temporal resolution of tens of picoseconds, and has a 2 mm diameter. The device comprises four metallic electrodes shaped like cups— a suppressor, an extractor, and an electrostatic einzel lens— all separated by thin polyimide (Kapton) insulation rings.

The microgun is designed utilizing a tungsten needle emitter configured in a Schottky geometry [11]. It gives a resolution of 1.3 ps at an energy of only 80 eV and a source-sample distance of 400 µm. The microgun is embedded in an electrostatic lens assembly (total outer diameter of 80 µm) of five gold electrodes – ground, gun lens, extractor, suppressor, and cathode electrode which has a nanometric tungsten tip (20 µm tip length, radius of curvature below 50 nm) (see Figure 9b). The entire structure is mounted at the edge of a glass slide. (see Figure 9a). After the generation of electron pulses, it is focused onto the sample using

an einzel lens made of the extractor electrode, lens electrode, and grounded aperture. The cylinder, which is composed of glass coated with silver, has a hole through which the photoemission pulse is focused onto the tip, protecting the diffracted electrons from the gun's stray fields. Gun electrodes are surrounded by a grounded metal-coated mica plate and a kapton cylinder, which makes it 80 µm of outer diameter.

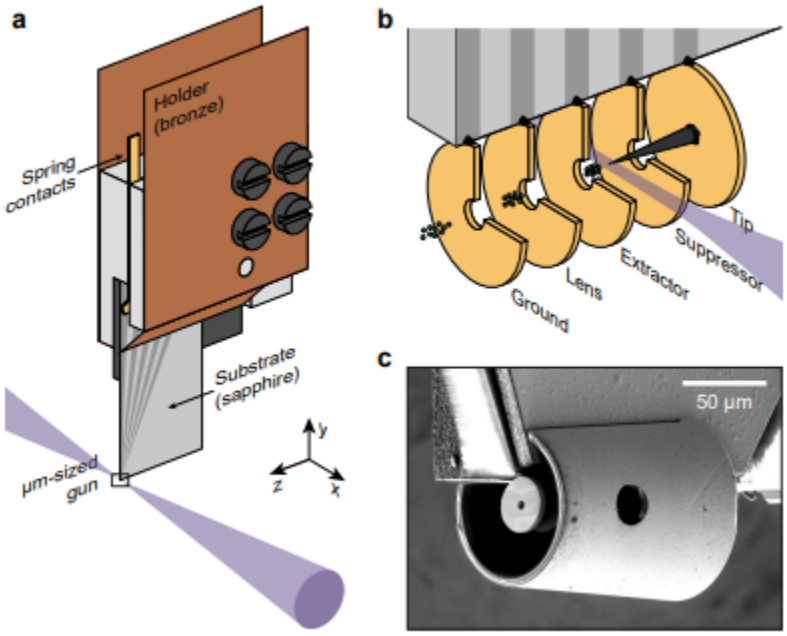

Figure 9: (a) Schematic drawing of microgun. (b) Schematic drawing of enlarged view of electron gun showing needle emitter and apertures. (c) Scanning electron micrograph of the micrometer-sized electron gun. Images are taken from Horstmann et. al. [10].

2.3 Material System

2.3.1 Silicon

Silicon or Si with an atomic number of 14 is in group 14 and period 3 of the periodic table. It is a semiconductor with an indirect band gap of 1.17 eV. At 0 K, silicon acts as an insulator. However, with an increase in temperature or the introduction of doping, the resistivity of silicon decreases, making it an efficient conductor. With a face-centered cubic Bravais lattice

Silicon	
Properties	Value
Crystal System	FCC
Lattice Parameter	0.54 nm at 295.7 K
Density	2.33 g/cm^3
Melting Point	1687 K

Table 1: Parameters of Silicon [13, 14].

and a lattice spacing of 5.42 $\mathring{A}$ at room temperature, silicon adopts a diamond cubic crystal structure [12]. This means that the atoms are sp^3 hybridized and bonded to four nearest neighbors in tetrahedral coordination. Owing to this covalent structure, it has a high melting point of 1687 K.

Various silicon surfaces - Si(111), Si(001), Si(110), Si(113) - show different surface properties depending on the cleavage plane. In this work, we use Si(001) as the substrate motivated by the work done by Hanisch-Blicharski et.al [8]. In their work, heat transport in ultrathin bismuth films on Si(001) is studied. Unlike Si(111), Si(001) has a simple and small unit cell restricting the reciprocal lattice vectors for momentum transfer [8].

Si(001)

When a silicon crystal is cleaved along the (001) plane, an ideal (1×1) surface of Si(001) results. In this structure, the atoms in the outermost surface layer are arranged in rows and bonded to second-layer atoms along the [110] or [$\bar{1}$10]direction, reducing surface energy [15–17]. The remaining two dangling bonds render each surface atom energetically unstable. One of the first and widely accepted models for the reconstruction of Si(001) was proposed by Schlier and Farnsworth in 1959. In their dimer model, the instability of the surface is reduced when adjacent rows of surface atoms undergo dimerization. This lowers the surface energy by decreasing the number of unsaturated bonds to single bond per atom [18]. Dimers are aligned along rows in the [110] direction, with adjacent rows displaced in opposite directions along the perpendicular [110] axis [19]. The resulting dimerization produces characteristic surface reconstructions such as the (2×1) and c(4×2) patterns(see Figure 10). The model was

further modified by Levine and Chadi, proposing that the dimers may be asymmetric, depending on the relative ordering of dimers.

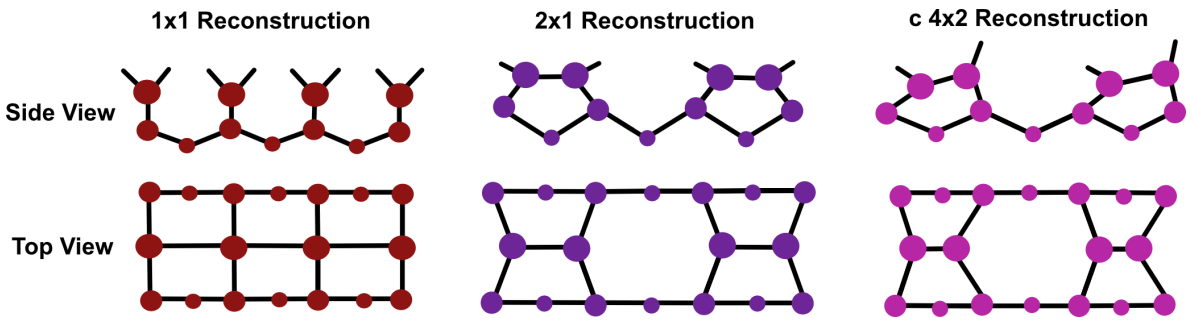

Figure 10: Reconstuctions of Si(001) surface.

The (2×1) pattern represents the regular arrangement of dimers along the rows. At temperatures below 200 K, this configuration transitions into the c(4×2) reconstruction through an order-disorder mechanism. The c(4×2) reconstruction is distinguished by buckling or tilted dimer model [20], where one atom in a dimer is slightly raised and the other slightly lowered, further stabilizing the surface by minimizing its electronic energy [21].

2.3.2 Bismuth

Bismuth is a semimetal with the element symbol Bi and atomic number 83. In the periodic table, it is in the 5th main group or nitrogen group.

In bulk form, Bismuth crystallizes with rhombohedral symmetry (see Figure 11). Each atom forms covalent bonds with three neighboring atoms, all positioned at equal distances. There are also three equidistant next-nearest neighbors. Another way to describe the structure is as hexagonal, where each unit cell contains six atoms, or as a pseudocubic arrangement, with a single atom in each unit cell.

Bismuth	
Properties	Value
Crystal System	Rhombohedral
Lattice Parameter	0.47 nm at 293 K
Density	9.79 g/cm^3
Melting Point	544.7 K

Table 2: Parameters of Bismuth [13, 14].

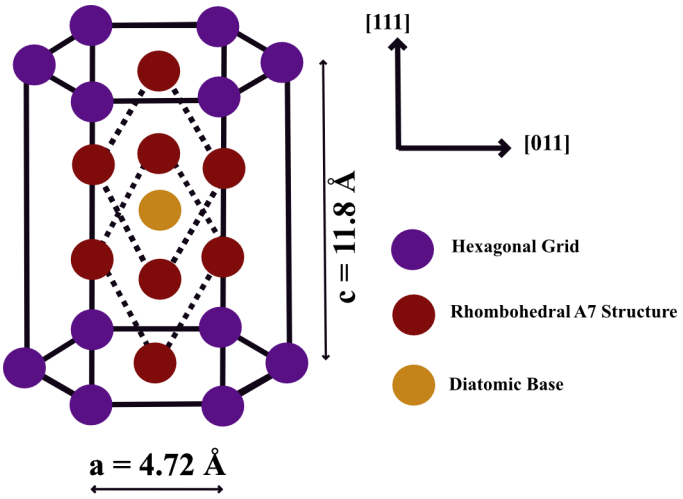

Figure 11: Unit cell of bismuth.

2.3.3 Bi(111) on Si(001)

The quasi-two-fold symmetry of Bi(111) arises from the superposition of two hexagonal domains rotated by 90° (see Figure 13a). This twinning is attributed to the Si(001) substrate's bilaterally symmetric structure [22]. The significant lattice mismatch between Bi(111) and Si(001) introduces substantial strain during growth. This strain is effectively alleviated through the creation of a periodic interfacial dislocation network, which serves to accommodate the difference in lattice parameters. Along the [110] direction, 11 Bi atoms, spaced 4.54 $\mathring{A}$ apart, align closely with the 13 Si atoms, which have a spacing of 3.84 $\mathring{A}$. In the [1$\bar{1}$0] direction, the atomic row separation of 3.93 Å in the bulk Bi(111) interface matches closely with the Si dimer spacing of 3.84 $\mathring{A}$. This is satisfied by a compression of the Bi film by 2.3 % (Figure 12) [23].

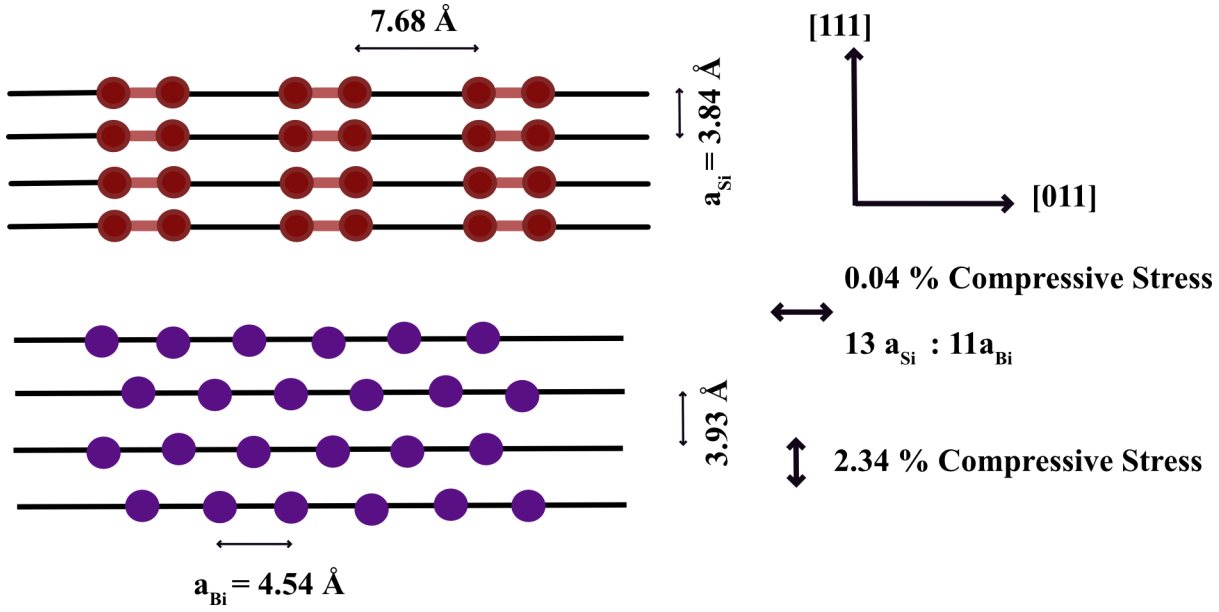

Figure 12: Bulk lattice matching of bismuth and silicon (Top view). Adapted from [22].

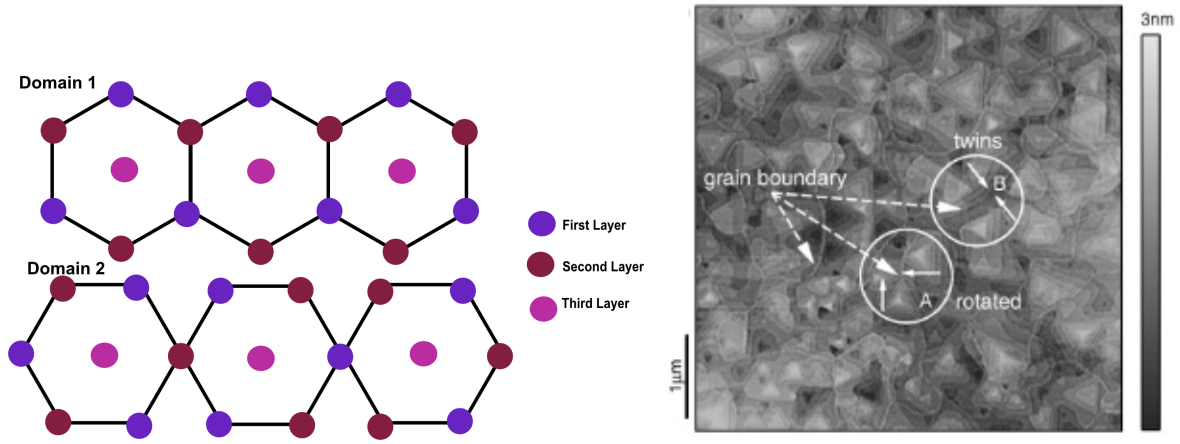

(a) (b)

Figure 13: (a) Real space representation of Bismuth on Si(001), where two domains rotated by 90^o is shown. Adapted from [24]. (b) An AFM image ($55, \mu m^2$) of a A 25 nm thick Bi film shows the alignment of neighboring Bi crystallites, which are demarcated by grain boundaries, indicated by dashed arrows within the circles. Circles A and B highlight Bi islands with a 90° rotation and areas displaying twinning, respectively. Taken from [25].

3 Results and Discussion

3.1 Preparation of bismuth films

Si(001) is initially degassed using direct current heating at 800°C for 3-4 hours. Subsequently, the silicon surface was pre-annealed at 900°C, flashed for 5 seconds at temperatures $T_{max} \geq 1250$°C, and subsequently post-annealed at 900°C. A pyrometer (Optris CTvideo 1MH) is used to track the surface temperature of the wafer as a function of current. This thermal cycle is typically repeated at least three times to remove oxide layers and to remove adsorbates from the surface. Figure 14a shows the resulting diffraction pattern of a flashed silicon wafer.

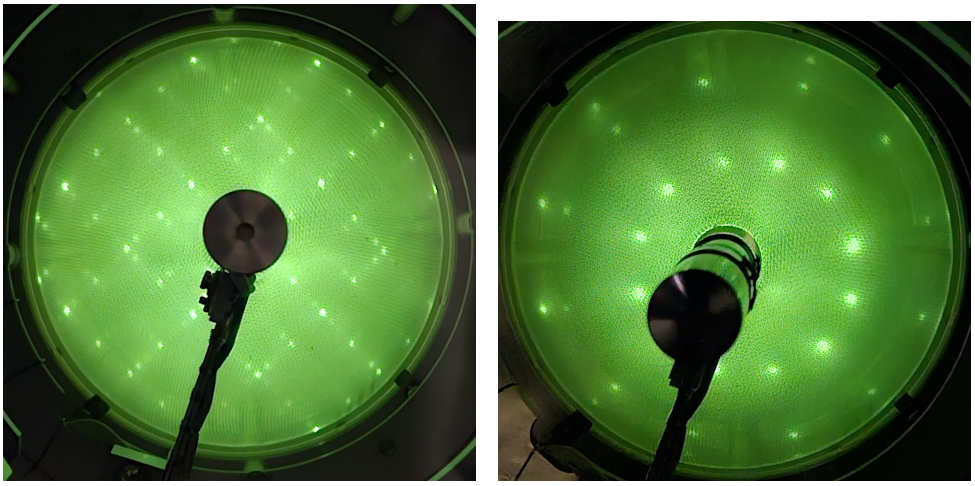

(a) (b)

Figure 14: (a) Diffraction Image of Si(001) in LEED at 85 eV electron energy. (b) Diffraction Image of Bismuth on Si(001) in LEED at 85 eV electron energy.

In order to deposit Bi(111) films on the silicon surface, we employ physical vapor deposition, which is a common technique to synthesize uniform films of high-purity materials. Bismuth films are prepared via thermal evaporation in ultra-high vacuum while maintaining pressures below 1×10^{-9} mbar to ensure minimal contamination. Specifically, we follow the procedure outlined in Ref. [22]. The deposition is performed at a substrate temperature of 150 K to avoid island formation. First, the flashed silicon wafer is cooled to 150 K prior to deposition.

During this cooling, the Si surface undergoes a reversible order-disorder phase transition at 200 K from (2x1) reconstruction to c(4x2) reconstruction (see Fig. 10). As surface reconstructions are generally sensitive to even small amounts of adsorbates, the observation of the c(4x2) structure is taken as an indication of a clean surface [22]. However, we could not see this reconstruction, which points towards a partial contamination of the surface from residual gases in the vacuum. There are also reports where electrons from the employed LEED gun induce disordering of the reconstruction at lower temperatures [26]. Supporting the crucial role of surface exposure, we observe that minimizing the interval between the final flash cycle and the commencement of bismuth evaporation is critical to preserve substrate cleanliness as adsorbates readily stick to the cooled surface.

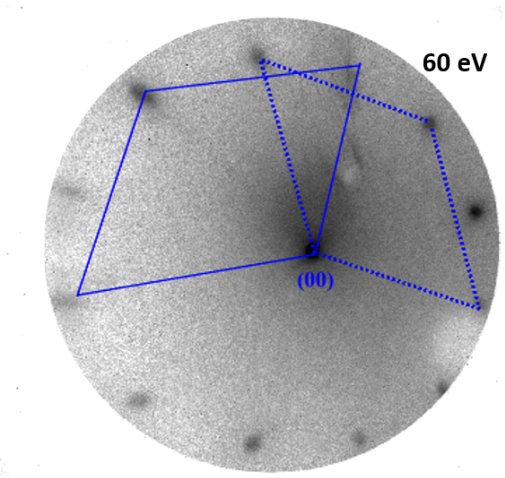

Figure 15: (a) Diffraction Image of 2 nm bismuth film on Si(001) taken using micrometer gun at 60 eV. Two domains rotated by 90° are shown.

At 150 K, the electron beam evaporator is used to deposit bismuth onto the silicon. The evaporation rate of the film is measured by a quartz crystal microbalance. At higher deposition temperatures, adsorbed bismuth atoms are mobile on the surface, thus increasing the probability of island formation. At lower temperatures, high surface roughness due to limited thermal diffusion makes the bismuth spots diffuse and weak [22, 27].

Post-deposition, the bismuth film is annealed at 220 K. Simultaneously, we track the LEED pattern of the bismuth film to monitor structural changes in the film. As reported by Bobisch et.al[28], a slight texture ring appears at low temperatures (Fig. 16), indicating the formation of a domain texture with random orientation. This ring disappears as we anneal to higher temperatures, indicating a thermally induced transformation of bismuth layers which increases the quality of the film. This thermal treatment reduces surface roughness and facilitates the creation of an interfacial dislocation network, which accommodates the lattice misalignment between bismuth and silicon [22]. Afterwards, the film is allowed to reach room temperature overnight.

Figure 14b shows the LEED diffraction pattern of a freshly prepared bismuth film on the Si(001) substrate. We observe 12 first-order Bragg spots, due to the overlap of two hexagonal domains rotated by 90° (see Section 2.4.3).

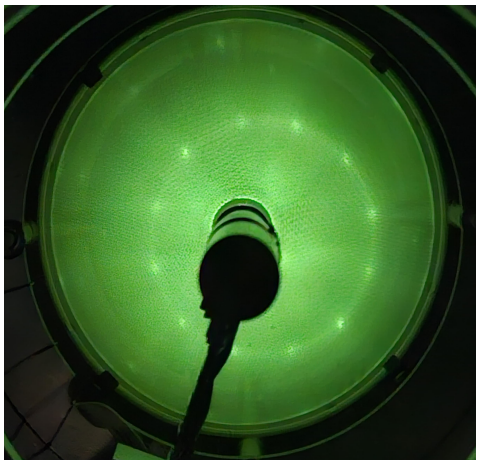

Figure 16: Diffraction Image of Bi(111) on Si(001) before annealing, showing a texture ring.

The pathway followed in obtaining a continuous and epitaxial bismuth film is depositing at 150 K and annealing up to 450 K [8, 22]. However, in our system, annealing at 450 K destroys the bismuth film, which manifests in the appearance of Si(001) diffraction spots even after annealing to only about 270 K. At the same time, annealing to 220 K and leaving the film overnight to reach room temperature does not destroy the bismuth film. We speculate on

the origin of this observation based on the possible deviation of the temperature reading at the manipulator and the actual sample surface temperature. The degradation of the bismuth film implies that the surface temperature far exceeds the nominal value and should be adapted accordingly in future experiments. In the present experiment, we have found the temperature at which dewetting starts (around 280 K) and have always made sure not to exceed this temperature. Observing the diffraction pattern during annealing confirms that the film is not dewetted.

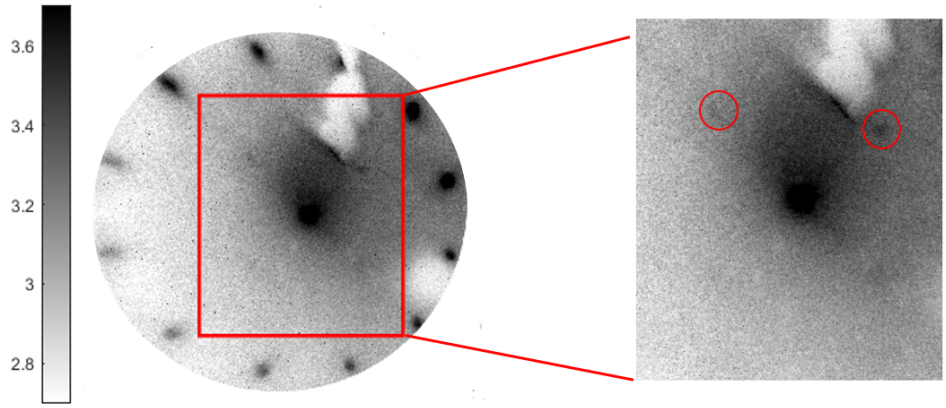

Figure 17: (a) Diffraction Image of a 1 nm film of Bismuth on Si(001) taken using the microgun (45 eV electron energy). Red circles indicate the silicon spots seen.

Bismuth films of various nominal thicknesses were prepared, ranging from 4 nm to 1 nm. All are uniformly deposited films except film of nominal thickness of 1 nm. Silicon spots were observed in the diffraction pattern of a nominally 1 nm thick bismuth film (Fig. 17 a) indicating that the bismuth might have been deposited in islands rather than in a uniform film. This observation is in agreement with Jnawali et al., where bismuth is reported to be deposited as islands below a coverage of 5.6 bilayers (2 nm). A specular intensity decrease in the initial stages of deposition due to scattering from adatoms or adatom islands is seen [29]. Beyond this thickness, bismuth deposition follows Frank-van der Merwe growth, where

a bilayer-by-bilayer growth is followed (Fig. 18) [22]. Upon further deposition, the density of adatoms reaches a maximum and islands of bismuth merge into a closed film. In all our measurements, we have made sure that the film is not dewetted or not too thin for exposing silicon surface.

We encountered many challenges during the preparation process outlined above. As discussed before, the time between the flashing of silicon and the deposition of bismuth significantly affects the quality of the bismuth film. However, controlling the time is challenging. After flashing the sample, which involves heating the sample to a high temperature, the sample is placed on the manipulator, which is at 150 K. There is a sudden and short jump in temperature due to this, which makes it essential to allow for some time for the temperature to stabilize. Also, it is crucial to give sufficient time for the evaporator to reach its required flux rate. Otherwise, the thickness deposited would be different from that calculated using the quartz microbalance since the initial rate was less. All these factors require a sufficient amount of time to be given between flashing and deposition.

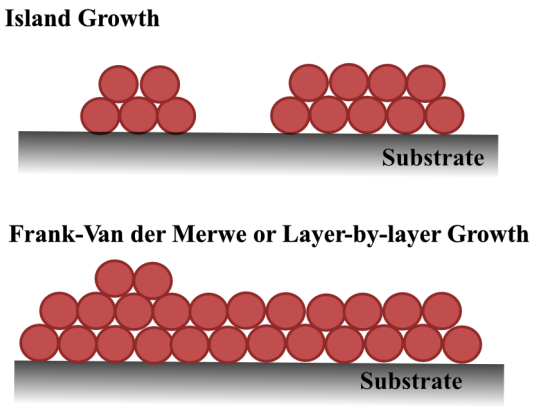

Figure 18: The top image depicts the formation of bismuth at thicknesses less than 2nm and the lower image depicts the bi evaporation by Frank-van der Merwe growth mode (adapted from [29]).

3.2 Bragg Spot dynamics

In order to study the ultrafast dynamics of bismuth films on Si(001), pump-probe measurements were carried out using the ULEED experimental setup. Here, we employ a 1030 nm wavelength pump beam, while probing the surface structure with electron pulses generated by the micrometer-sized gun. In this experiment, we analyze these diffraction patterns to study the ultrafast dynamics of the prepared sample.

Figure 19 shows the diffraction pattern of a 4 nm thick bismuth film taken with the micrometer gun at an electron energy of 60 eV at 30 K. Aiming for the clearer detection of the underlying dynamics of a sample, we do the measurements at lower temperature since there is less thermal excitation. Cooling is done with liquid N_2 to 80 K or with liquid He to 30 K. After cooling, we make sure that there is temporal and spatial overlap between the pump and the probe. Temporal overlap is determined by assessing the stage position at which the intensity reaches half of its value when pump beam is applied. This stage position is taken as t_o, which is where the pump and probe reach the sample at the same time. Diffraction spots are recorded by moving the sample to one side till it vanishes. The position at which the pattern vanishes is marked. The same procedure is done in the opposite direction and marked. The marked line becomes the area for spatial overlap.

Diffraction images at different time delays ranging from -50 ps to 2800 ps were taken with an integration time of 30 s each. A pump beam with a fluence ranging from 1.27 mJ cm^{-2} was directed at the sample.

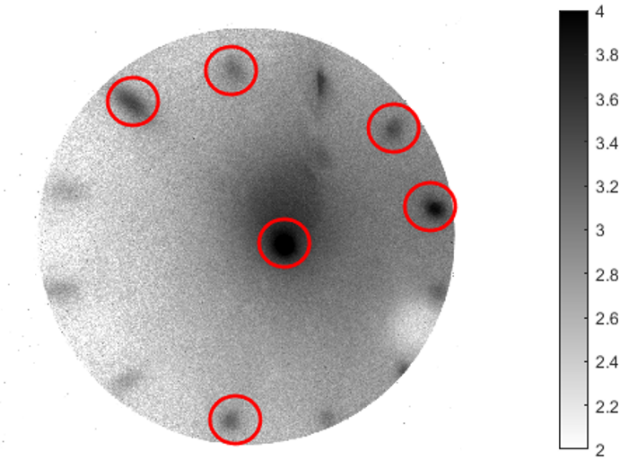

Figure 19: (a) LEED Image of Bi on Si(001) with 60 eV gun energy at 30 K. Bragg spots selected for analysis are marked.

To capture the temporal evolution of only the Bragg spots and to eliminate other background effects, a circular mask is used. These are employed to select diffraction spots of sufficient intensity and good signal-to-noise ratio. The selected area is then subsequently analyzed for all time delays, and spot intensity values at each of the spots at each time delay are obtained. The diffraction spot intensity values obtained from this are then normalized with the intensity of the spots before optical excitation. The time-dependent variation of the spot intensity with pump excitation is analyzed to extract the associated time constants. Figure 19 shows the 6 Bragg spots selected for analysis in all the time delays. The negative logarithm of the normalized intensity gives a measure of the temperature of the Bi film, as evident from the Debye-Waller factor. This is then fitted with:

$$-ln(\frac{I(t)}{I_0}) = a\left(1-exp(-(\frac{t-c}{\tau_1}))\right)\left(exp(-\frac{(t-c)}{\tau_{cool}})+e\right)(t>c) \tag{21}$$

where I(t) is the intensity at time t, and I_0 is the initial intensity. The first term and the second term represent the rise and decay of the intensity curve, respectively. The rise time τ_1 is the time required for the intensity to decrease or the time with which the temperature of the film

rises when the pump arrives. a denotes the amplitude of the temperature rise. The cooling time constant τ_{cool} is the time required for the temperature equilibration of the bismuth film with the silicon substrate. The parameter c is related to the time offset, and e is a constant that likely affects the offset or baseline behavior of the decay.

The time-dependent normalized diffraction spot intensity of the same film described above is plotted in Figure 20. A 30% intensity suppression within 100 ps is observed in the figure. The maximum suppression is observed around 90 ps, followed by a slow recovery on a ns timescale. The time-dependent temperature drop of diffraction spot intensity due to the Debye-Waller effect is plotted in Figure 21. From the fit, we obtain the rise time as 27.62 $\pm$ 1.57 ps and the cooling time constant as 556.7 $\pm$ 27.2 ps.

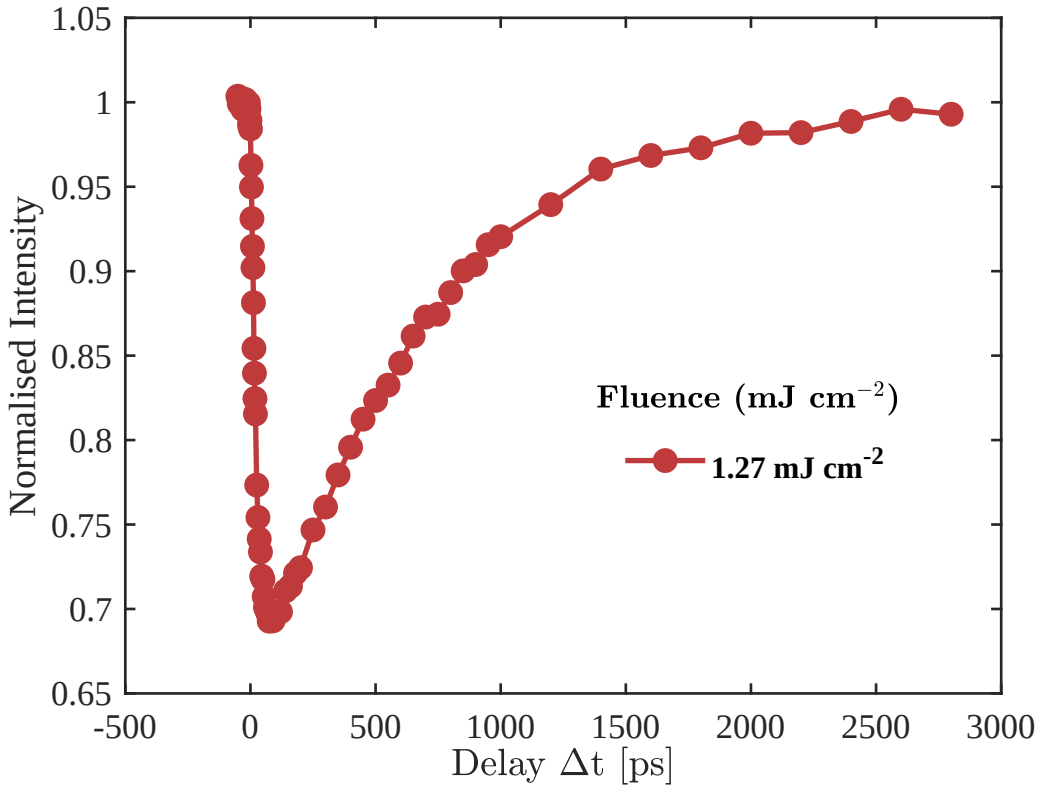

Figure 20: Pump-probe time delay scan taken with a pump fluence of 1.27 mJ cm^{-2} and electron gun energy of 60 eV.

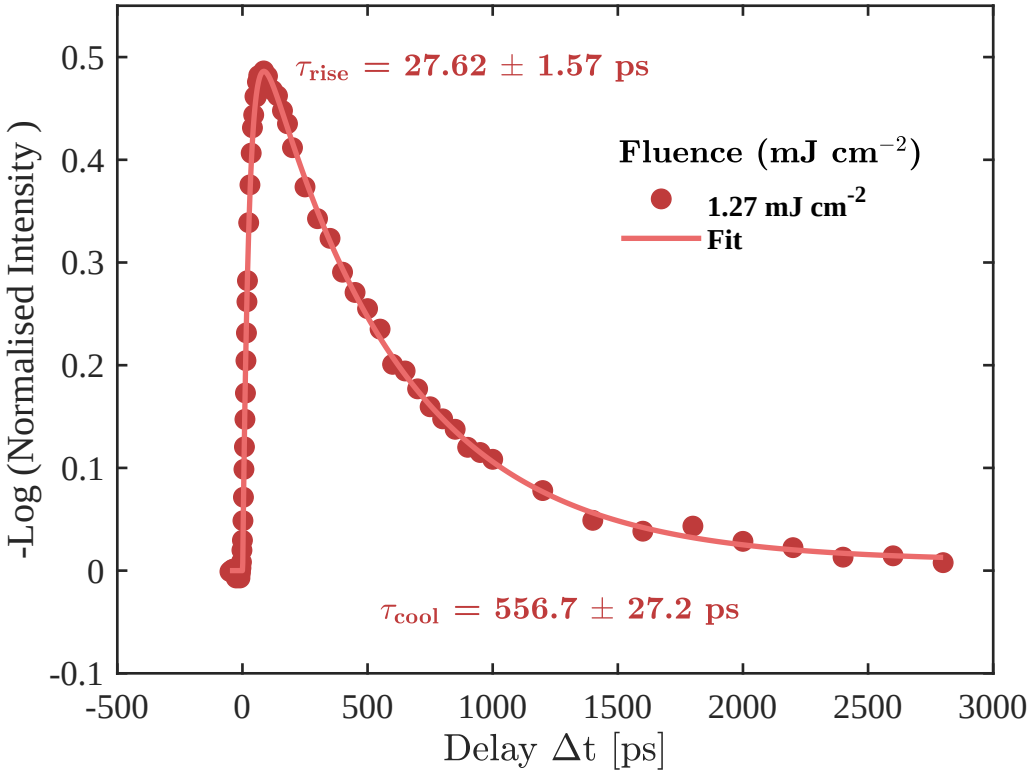

Figure 21: Corresponding graph of negative logarithm of normalized intensity versus time delay graph.

Discussion

We find the above results in generally good agreement with existing literature. Brand et. al. report a fast and a slow component of intensity decrease when the pump excites a 4.5 nm thick bismuth film [30]. The fast component with a time constant τ_1 = 5 ps (independent of base temperature) is attributed to electron-phonon coupling, while the slower component with a time constant τ_2 = (97 ± 18) ps at 30 K is attributed to the thermal activation of the pristine Bi film surface resulting from the interaction between bulk and surface phonon modes. In the above measurements, we could not see the faster component, probably due to lower temporal resolution of our experimental setup. The fitting worked best for single-exponential behavior and thus excluded the need for fitting with double-exponentials to observe the two components. The observed rise time thus compares well with literature results, when considering only a single time constant.

3.2.1 Fluence dependence

Results

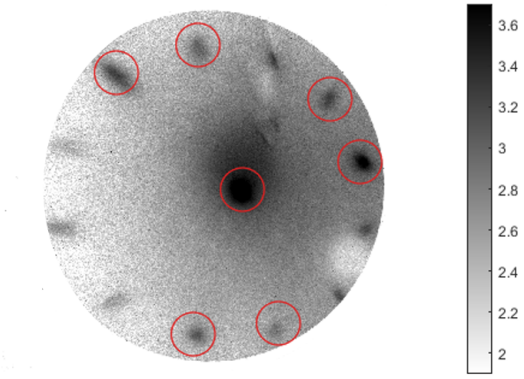

Figure 22: (a) LEED Image of Bi on Si(001) using 60 eV gun energy . Bragg spots selected for analysis for all the fluences are marked.

A set of time-resolved measurements was taken on a 4 nm thick bismuth film with fluences ranging from 1 mJ cm^{-2} to 2 mJ cm^{-2}. The delay scans for different fluences are depicted in Figure 23. All measurements were taken at 30 K and 60 eV electron energy. The integration time was 10 seconds for 3 images in a single time delay position. Bragg spots, selected for analysis, are shown in Figure 22. Figure 24 compares the rise times for different fluences. Here, higher fluences lead to a larger suppression of intensity when the pump beam reaches the sample. With increasing fluence, the rise time seems to decrease. This can be due to increased electron-phonon coupling due to more excited electrons speeding up the rise in temperature [30]. The cooling time constants for different fluences are also compared in Figure 25, and it shows no apparent dependence on the fluence.

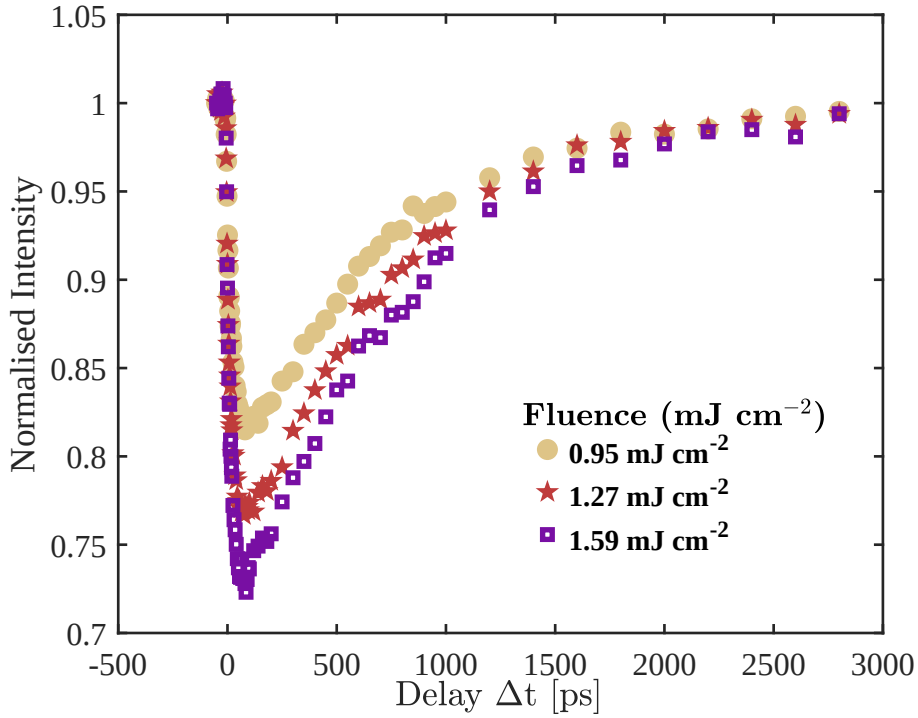

Figure 23: Pump-probe time delay scan taken for different fluences with electron gun energy of 60eV.

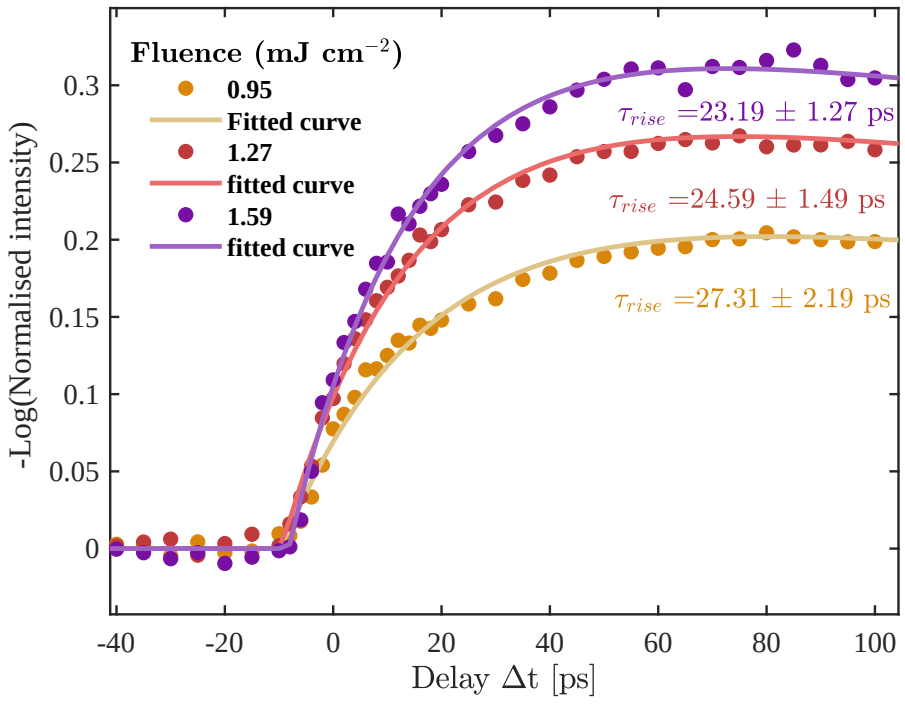

Figure 24: Comparison of rise times for different fluences.

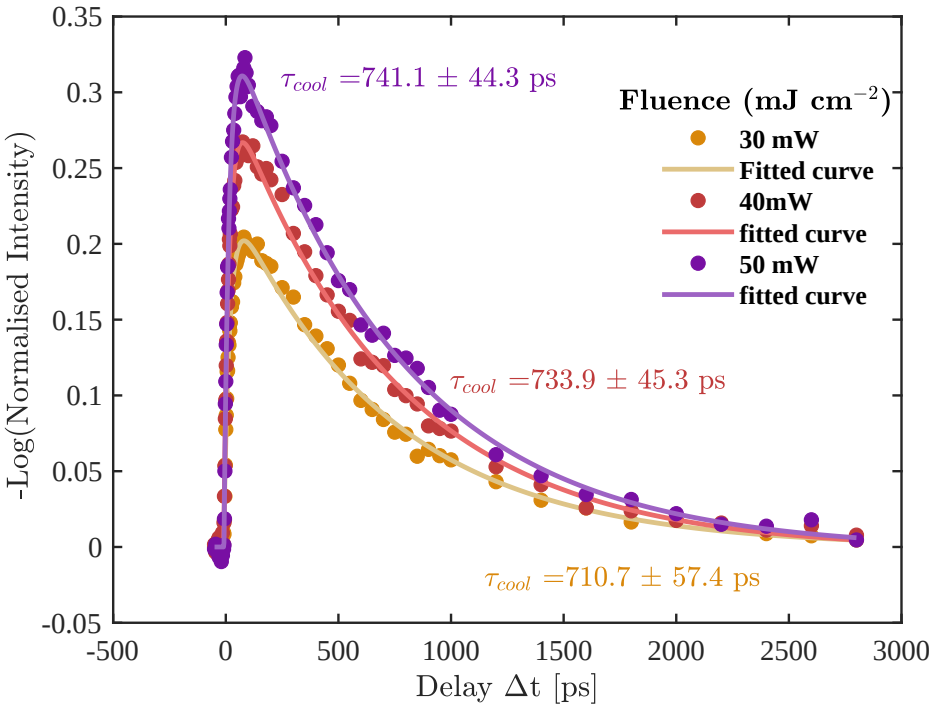

Figure 25: Comparison of cooling time constant for different fluences.

Another set of measurements was taken on the same film on a different day (see Figure 26). In this data, however, the above-described dependence of fluence on rise time was not observed (see Figure 27). But, the cooling time constant shows the same trend as in the previous set of measurement (see Figure 28), reinforcing the fluence-independent cooling time constant behaviour.

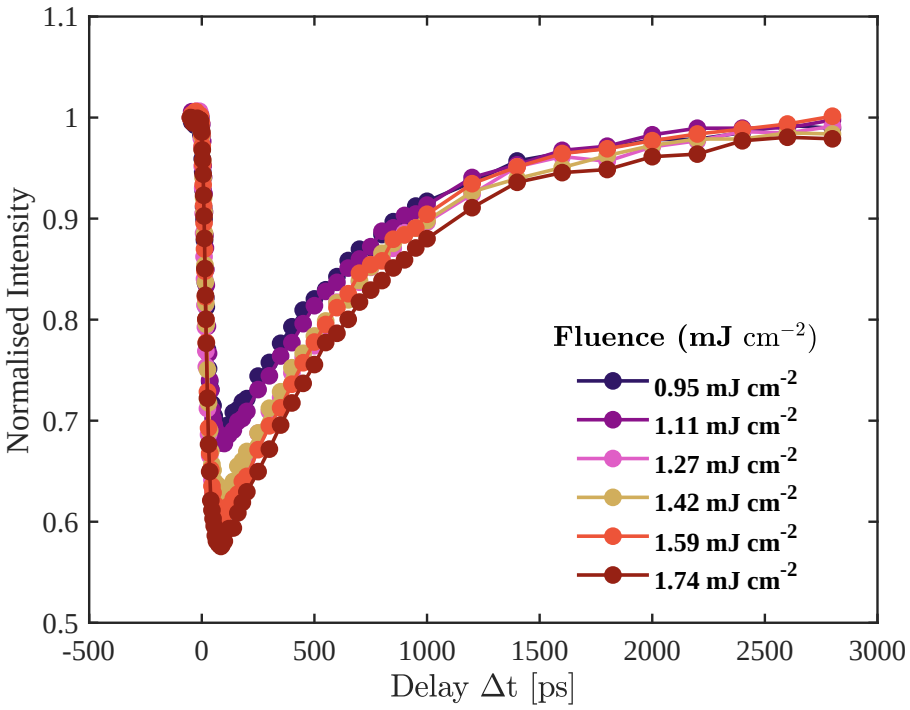

Figure 26: Pump-probe time delay scan taken for different fluences with electron gun energy of 60 eV - data set 2 .

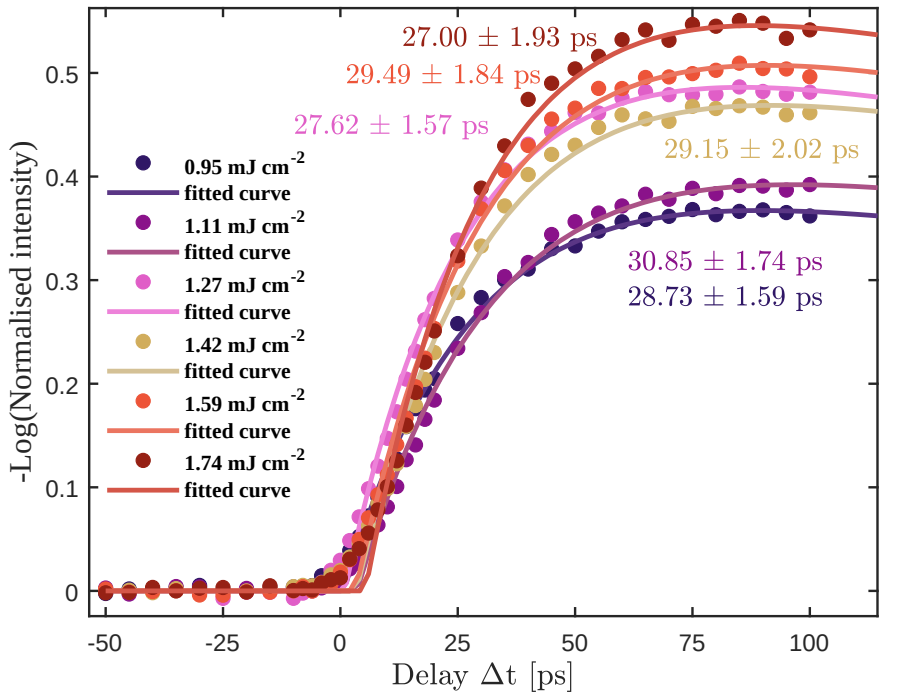

Figure 27: Comparison of rise times for different fluences - data set 2.

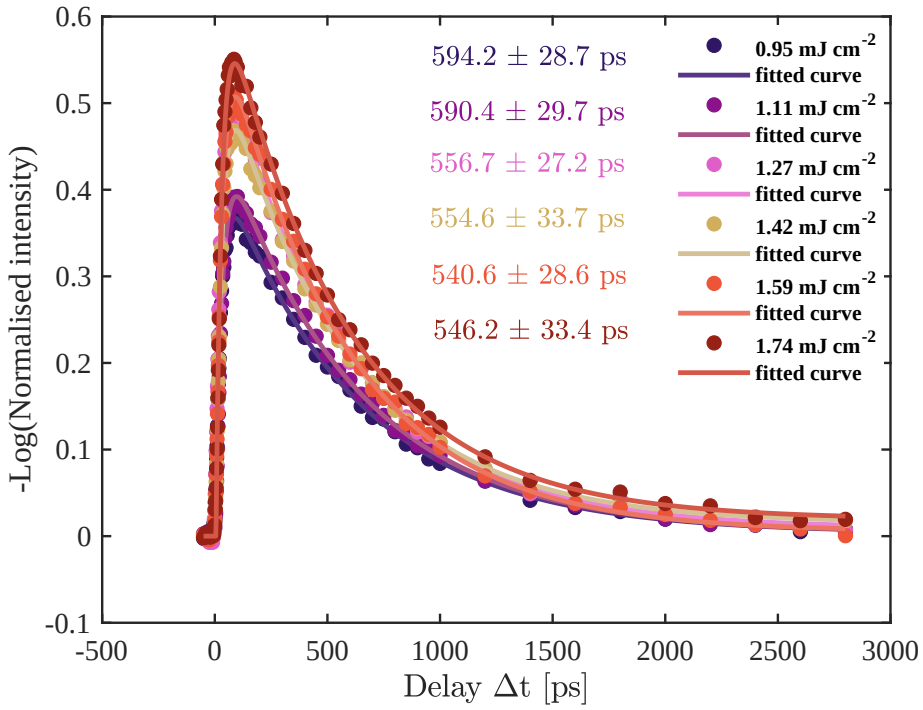

Figure 28: Comparison of cooling time constants for different fluences - data set 2.

Discussion

Decreasing rise times with fluence in this experiment (see Fig. 24) are in agreement with the trend reported by Brand et al. [30], where the rise time was found to be inversely dependent on the maximum temperature attained when the film is excited. In their work, the slow component of the intensity decrease is attributed to energy transfer between bulk and surface phonons. Generally, the excitation time constant is derived from thermal conductivity of the bulk sample. Since thermal conductivity is strongly influenced by phonon-phonon interactions, particularly Umklapp scattering at high temperatures, analyzing its temperature dependence helps explain how efficiently bulk phonons couple to surface phonons. A good agreement between experimental data and the data derived from thermal conductivity confirms the inverse temperature dependence. However, we could not see this trend in the second set of observations in figure 27. At higher maximum temperatures, the reduction in rise time is small due to the above-described inverse dependence. In that case, we could suppose that the large variations in rise time in figure 27 were not seen due to this fact. At the same time,

it is evident from the time delay curves that the increase in suppression was not uniform for the applied fluence.

In both sets of measurements, the cooling time constant is independent of the fluence (figure 29b). This is in strong agreement with Hanisch-Blicharski et al. [31]. The reason behind this statement is explained as follows:

$$\tau_{cool} = \frac{c}{\sigma_k} d \tag{22}$$

where c is the specific heat capacity, and d is the film thickness. The thermal boundary conductance σ_k is given by [7];

$$\sigma_k = \frac{1}{2} \int_0^\infty c(\omega, T) < v_z(\omega) >< t(\omega) > d\omega \tag{23}$$

where c $(\omega, T), v_z(\omega), t(\omega)$ is the specific heat capacity of phonons of frequency ω, average phonon velocity perpendicular to the interface, and phonon transmission phonon probability respectively. Here, the assumption is that the heat transport across the interface is only mediated by phonons. Temperature dependence of τ_{cool} due to the factor σ_k is canceled out by the term $c(\omega, T)$ in equation 22 [7].

An interesting observation in the two sets is the value of the cooling time constant, 741.1 $\pm$ 44.3 ps in the first set (figure 25) and 540.6 $\pm$ 28.6 ps on the same film but on a different day (figure 28). One possible cause for this discrepancy could be the degradation of the sample surface by adsorbates. However, the Bragg spot intensity did not decrease, indicating that this may not be the reason. Spatial variations in the homogeneity of the probed area can be another reason.

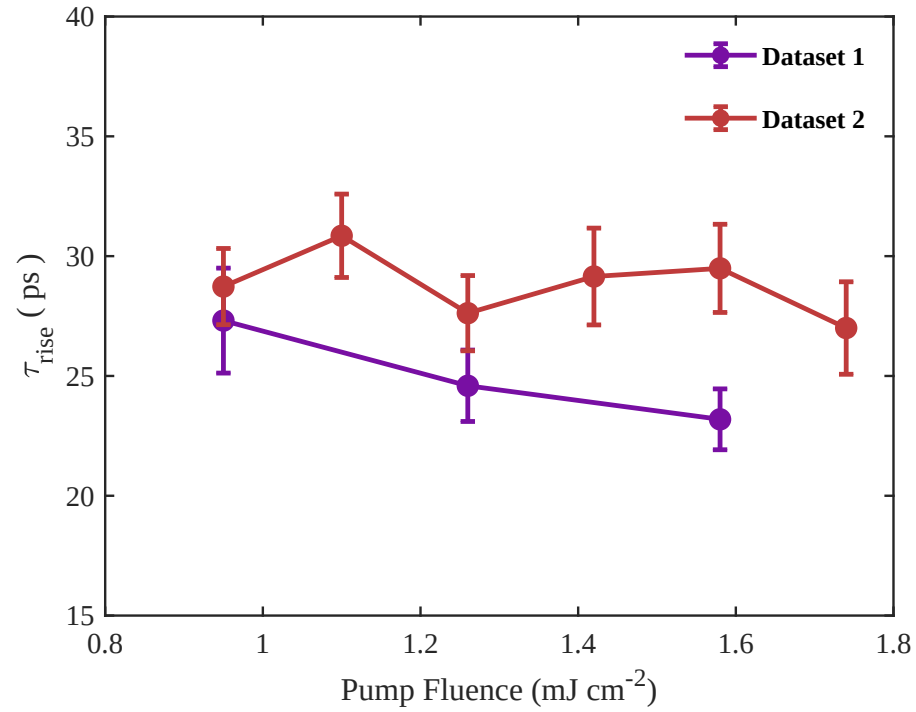

(a)

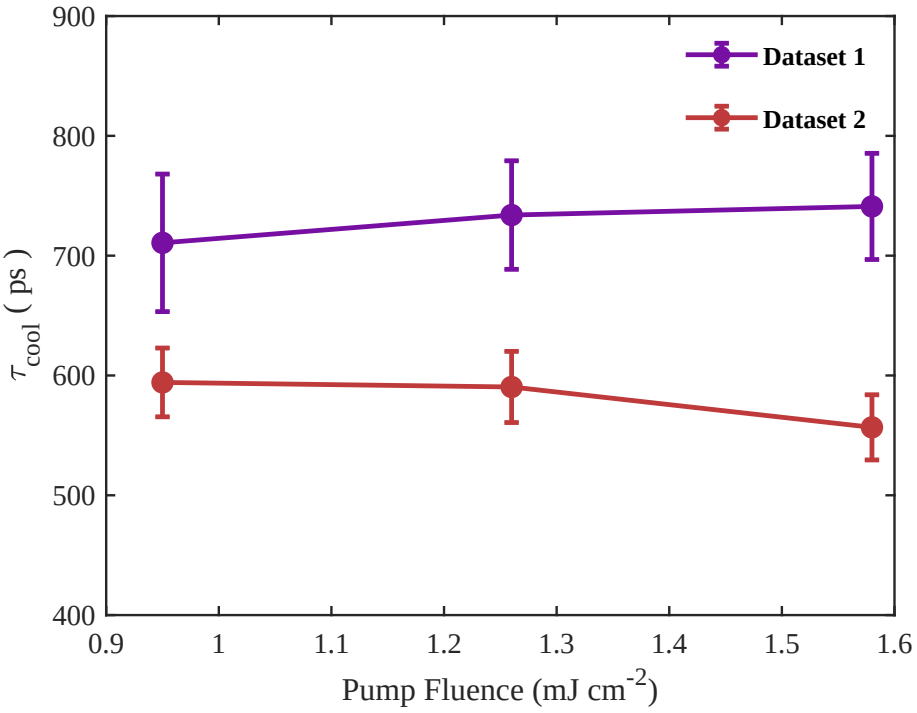

(b)

Figure 29: (a) Rise time plotted for different fluences. (b) Cooling time constant plotted for different fluences.

3.2.2 Charging

Figure 30 shows time-dependent spot intensity curves of the (00) spot and two first-order spots. It is clearly observed that the intensity does not recover back to the initial value. The same issue is observed in the case of the (00) spot intensity for different fluences (Figure 31a). Curves were found to not recover back to their original values, either falling below or exceeding the intensity before time zero. Figure 31b shows that the issue seems to be evident even when using different electron energies. It is also observed that the (00) spot intensity always overshoots the initial intensity when an electron beam of 60 eV is used while the intensity of all first-order spots is less than the initial intensity. However, the trend seems to be different when a different electron energy is used.

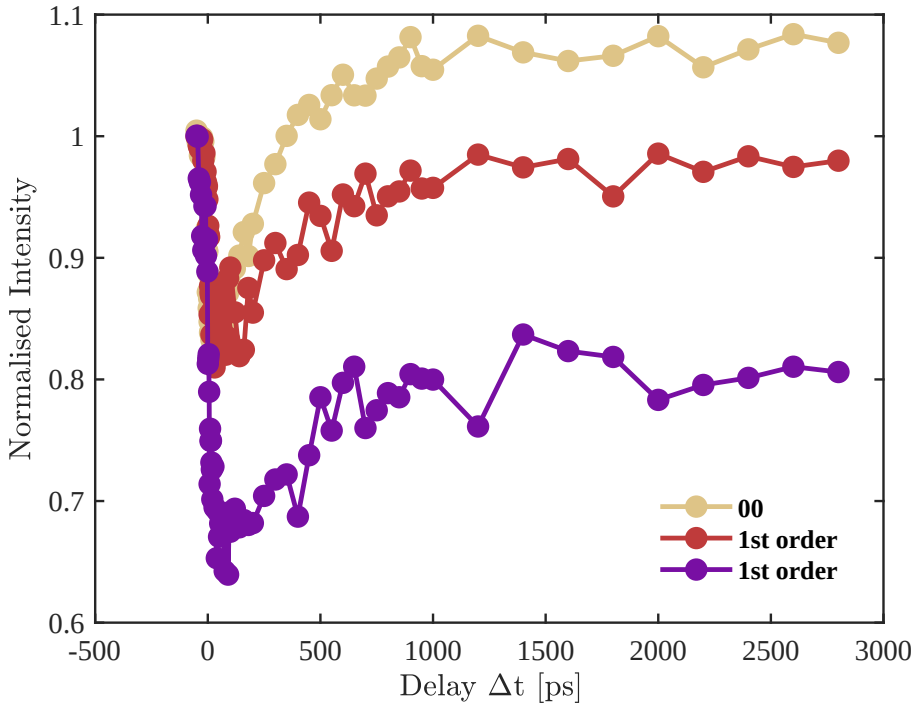

Figure 30: Normalized intensity versus time delay for different Bragg spots using 60 eV electron energy.

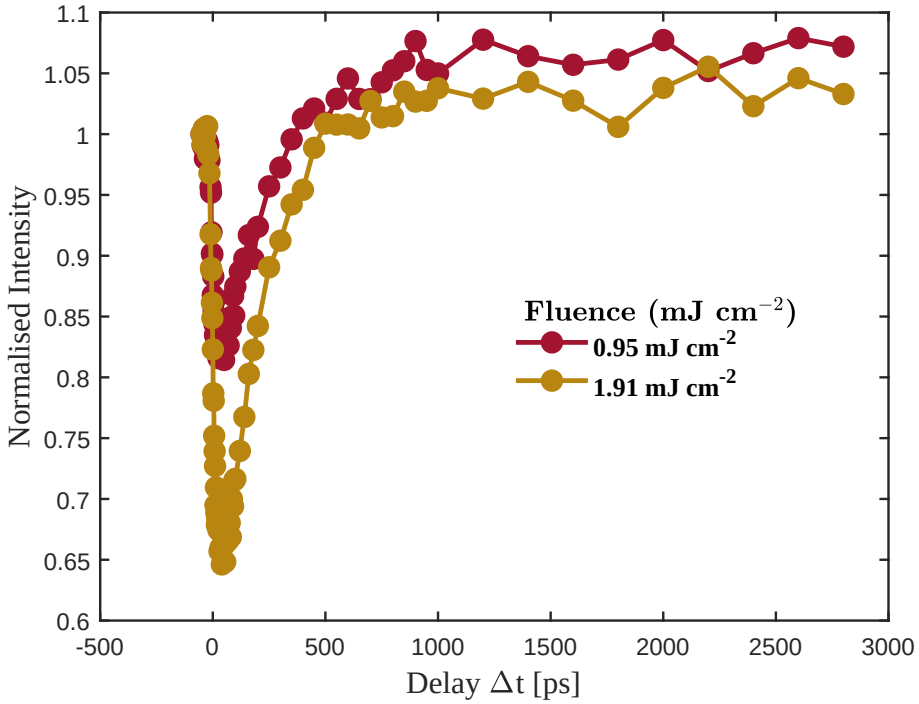

(a)

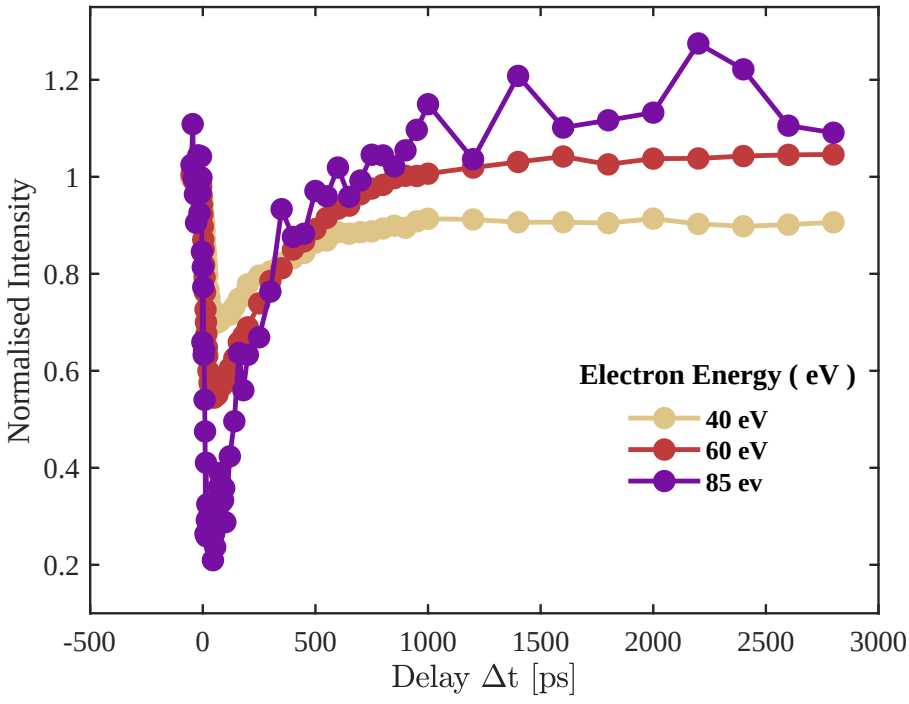

(b)

Figure 31: (a) Normalized intensity versus time delay of the (00) spot for different fluences using 60 eV electron energy. (b) Normalized intensity versus time delay of the (00) spot for different gun electron energies.

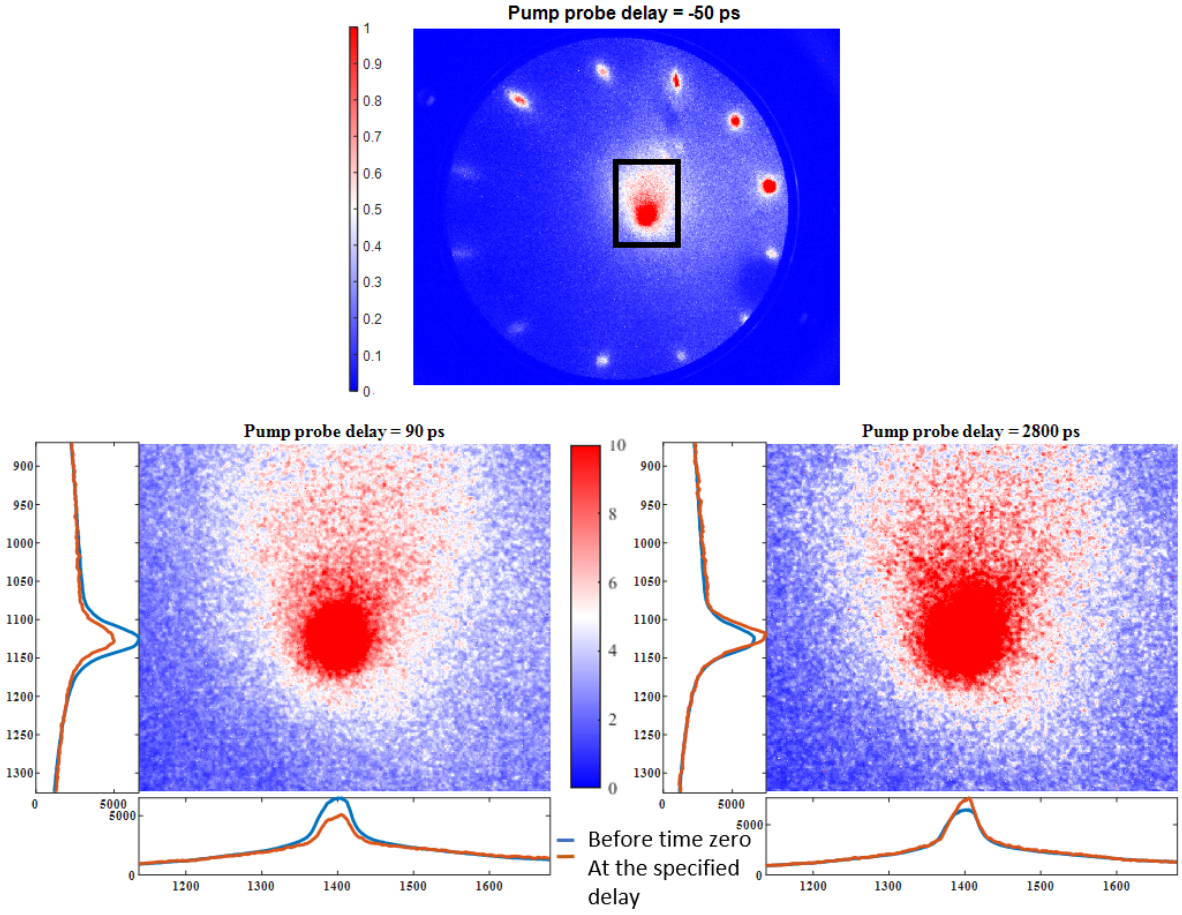

Figure 32: Image showing the change in spot profile of (00) Bragg spot.

Discussion

Figure 32 shows a slight shift of spot position with relative time delay which can be an indication of the possible distortion due to charging. Maximum intensity at 2800 ps exceeds the intensity before time zero for the (00) spot at an electron energy of 60 eV. At 90 eV, a small change in spot shape is also evident, possibly due to charging. The sample cannot dissipate photoexcited charge carriers, resulting in the formation of a space charge cloud. The resulting electric field acts as a screening shield, distorting the incident electron beam, which in turn affects the diffraction pattern [32]. Reshuffling of intensity between the (00) spot and first-order spots, as evident in Figure 30 can be an indication of change in effective electron energy. Differences in the distances between Bragg spots on the left and right sides of the

diffraction image might also point to the same problem. Bragg spots on the right are closer than those on the left side.

The distortion still remained even after reducing the pump power. Another possible solution can be using a silicon wafer with higher conductivity.

3.2.3 Thickness dependence

In order to study the dependence of thickness on rise and cooling time constants, Bismuth films of thicknesses 1.5 nm, 2 nm, 3 nm, and 4 nm were prepared. Measurements were conducted at a base temperature of 30 K by cooling with liquid Helium. The pump fluence and electron energy were set to 1.59 mJ cm^{-2} and 60 eV, respectively.

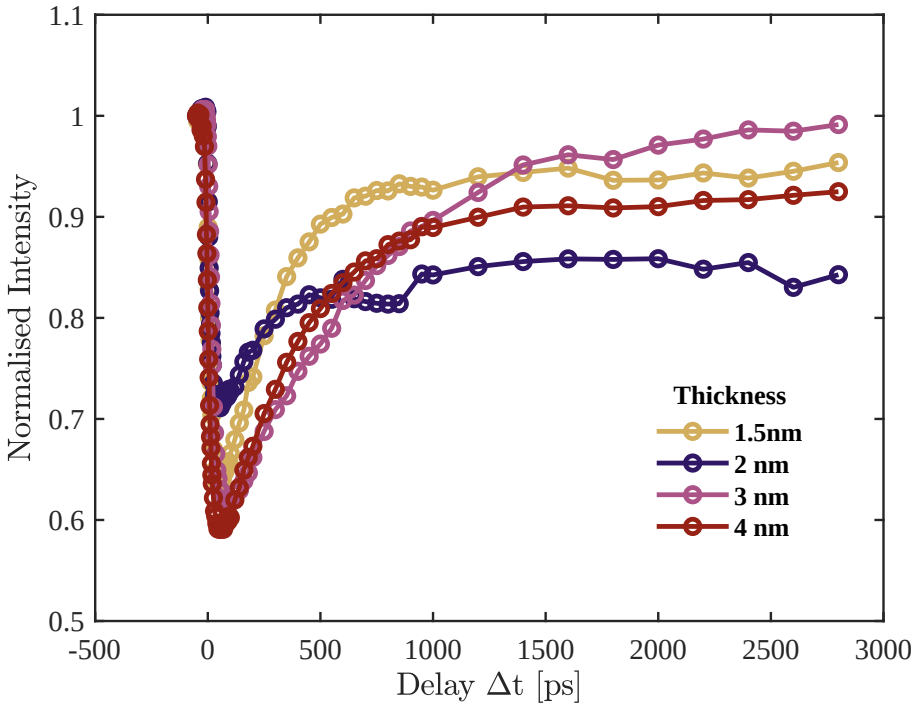

Figure 33: (a) Delay scans for different thicknesses with pump fluence and electron energy set to 1.59 mJ cm^{-2} and 60 eV.

Time-dependent intensity scans for different thicknesses are given in Figure 33. Variation of cooling time constant with respect to the thickness of bismuth film is plotted in Figure 34.

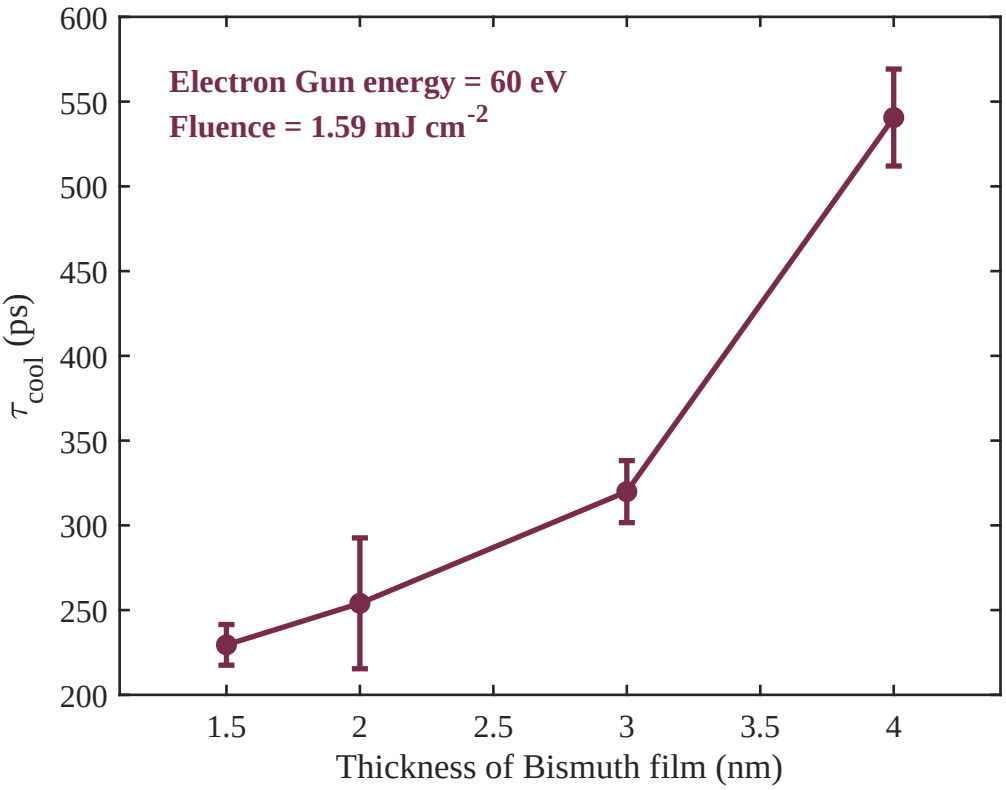

Figure 34: (a) Cooling time constant for different thicknesses.

Discussion

From equation 21, it follows that the cooling time constant is linearly dependent on the thickness of the film [31]. From Figure 34, it is evident that the cooling time constant increases with thickness.

Bobisch et al. report that for thicknesses of the bismuth film of less than 6 nm, a deviation from linear dependence between thickness and cooling time constant is observed [28]. When phonons attempt to move through the interface of a thin film with a thickness less than the mean free path [33], a realization of total internal reflection can be observed. When the angle of incidence of these phonons is less than the critical angle of total internal reflection, these phonons can move out of the film and cause heat transfer (Figure 4). However, a reduced transfer rate was observed when the angle of incidence was larger than the critical angle (see

Figure 5). In our experiment, a shift in trend after 3 nm is very evident as compared to cooling time constant values below 3 nm. However, we have very few data points to confirm a linear dependence between thickness and cooling time constant above 3 nm.

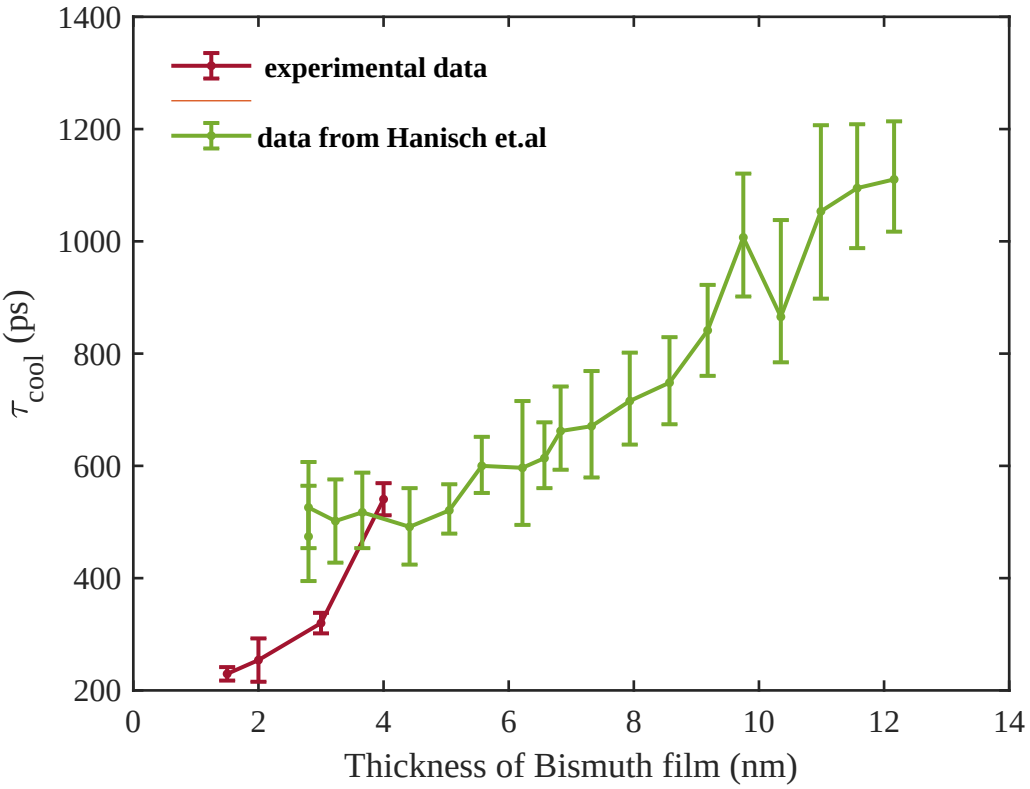

Figure 35: (a) Cooling time constant for different thicknesses compared with [28].

Comparing the experimental results of the above, a discrepancy in the values of cooling time constant for each thickness is seen in Figure 35. Firstly, they do not prepare thicknesses less than 4 nm. However, we could prepare even thicknesses down to 1.5 nm with no indication of a broken-up film, manifesting in the presence of silicon spots in LEED. G. Jnawali reports that films with thicknesses less than 2 nm show islanding [29]. This variation can be due to the deposition rate calibrated by the quartz crystal microbalance. As discussed before, we could prepare a bismuth film of thickness 1.5 nm. However, islands of bismuth films are observed for thicknesses less than 2 nm [29]. This points to the fact there is a slight offset

to the thickness calibration in our experimental setup. Another observation that supports the above claim is the thickness at which a deviation from the linear behaviour is seen. In our experiment, we see the deviation starts below 3 nm, whereas in Hanisch-Blicharski et al., the deviation is seen below 6 nm. Secondly, the cooling time constants in our experiments are smaller than the values reported in [28]. The minimum cooling time constants reported by Hanisch et al. are on the order of 400 ps. However, we observe 200 ps of cooling time constant in a 2 nm thick film.

3.3 Background Dynamics

When an electron beam interacts with a sample, electrons are inelastically scattered due to the interaction with the material. Studying the resulting diffuse background provides insights into the transient phonon population and lattice dynamics [6, 34–36]. The scattering vector represents the change in crystal momentum during a scattering event and is directly proportional to the momentum of the phonon which gives a measure of the distribution and population of phonons. Analyzing these patterns allows for extracting phonon populations and lifetimes.

In this study, we investigate the background dynamics of ultrathin films and compare them to relatively thicker films. As previously discussed, phonons in thin films quickly escape the film, whereas phonons in thicker films have sufficient time to scatter and repopulate the critical cone. Our goal is to determine if this phenomenon is observable in the diffuse background of the films. Here, we analyze the background dynamics of ultrathin films and compare it with a relatively thicker film.

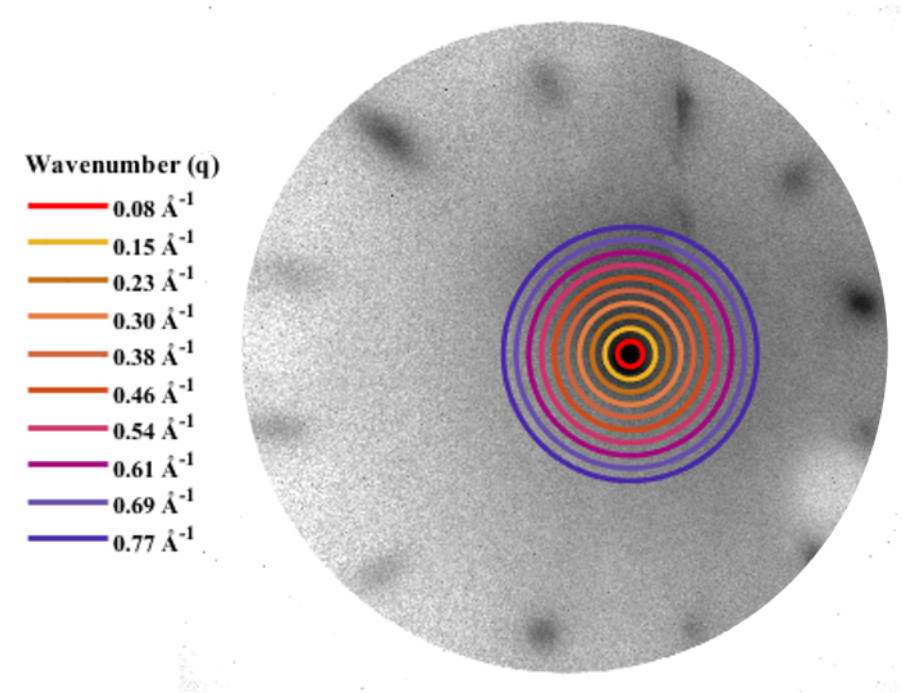

Figure 36: Concentric rings plotted in the Brillouin zone around (00) Bragg spot.

To investigate the phonon dynamics, we analyzed the diffuse background of a diffraction pattern of 1.5 nm and 4 nm thick bismuth films taken with an electron energy of 60 eV. By drawing concentric rings of equal width around the most intense Bragg spot within the Brillouin zone, we examined phonon populations across specific momentum transfer (q) intervals (figure 36). The image was taken over a duration of 30 seconds and with a pump fluence of 1.58 mJ cm^{-2}. The size of the Brillouin zone is calculated from the distance separating the (00) spot from the first-order diffraction peaks. Since the location of first-order Bragg spots is distorted in the LEED pattern, we consider an average across all spot positions. We analyze the radial distribution of electron intensities around Bragg spots, which integrates phonon contributions with specific wave vector $|\vec{q}|$ across the surface Brillouin zone. 10 rings with increasing radius of 0.08 $\AA$ (rings of the same width) are drawn. This allows us to understand

the phonon population in a certain interval of q. In each of the rings, the mean intensity is normalized by the intensity before time zero. Figure 37 shows the temporal evolution of the normalized intensity in the nine rings (excluded the innermost ring) for a 1.5 nm bismuth film.

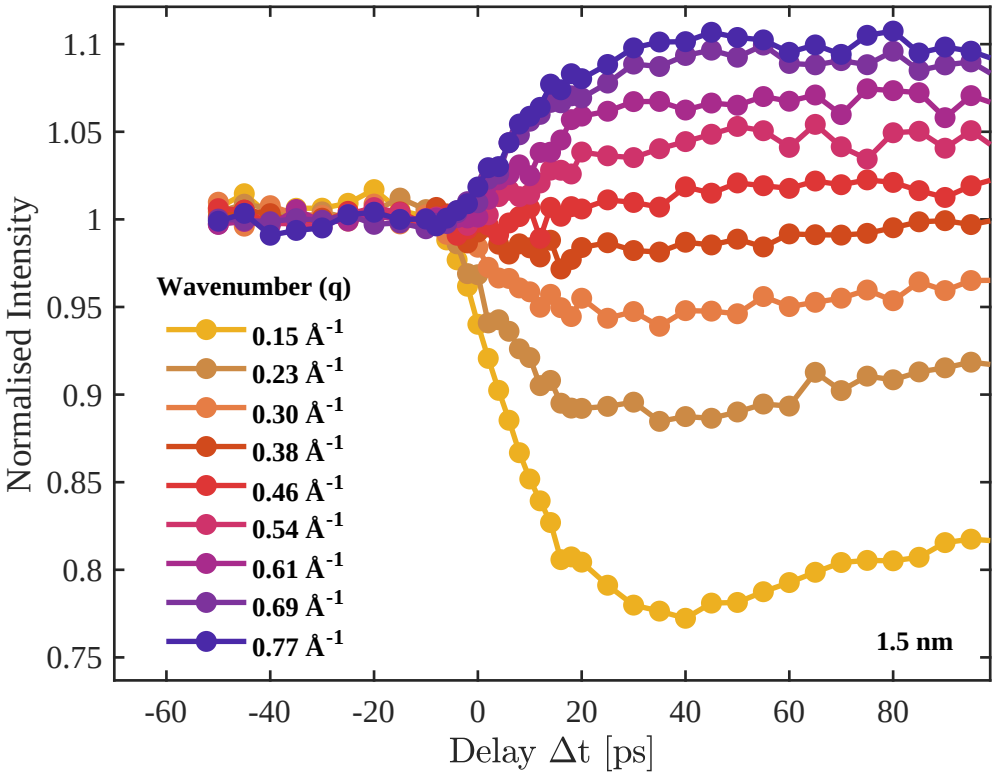

Figure 37: Temporal evolution of the normalized intensity in the nine rings for a 1.5 nm bismuth film.

The dynamics of the Bragg spot are revealed by the innermost rings, while more of the phonon dynamics are revealed by the outer rings. The observed rapid intensity decrease in the innermost rings corresponds to Bragg spot suppression, due to the Debye-Waller effect. However, in the outer rings, a more complex behavior is observed, where the intensity initially drops but shows a slight increase at larger delays. The initial intensity drop is due to the contribution from the Bragg spot. As we move towards the zone boundary, we can see that the amplitude of the initial drop decreases until it vanishes. The intensity increase is due

to the inelastic scattering of electrons.

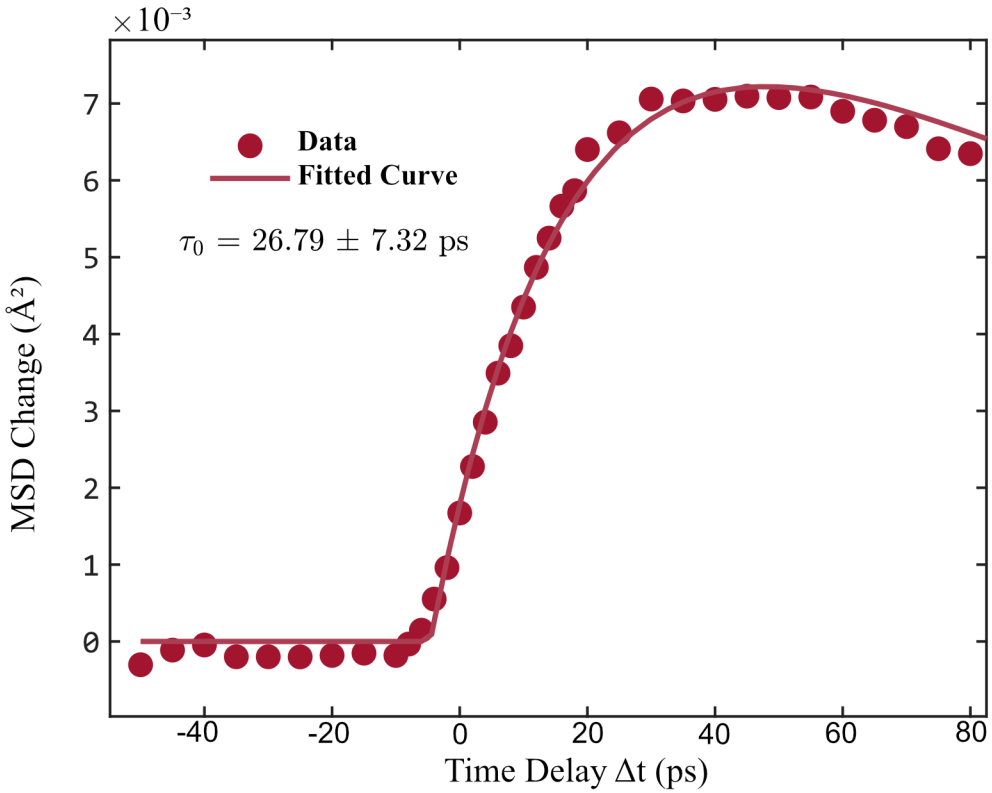

Figure 38: Temporal evolution of MSD for 1.5 nm bismuth film.

To extract momentum-resolved rise times from all these areas of background, firstly, we find the out-of-plane mean square displacement (MSD). The out-of-plane MSD quantifies the average squared deviations of atomic positions perpendicular to the material's surface over time. When any perturbation, such as laser excitation, occurs, perpendicular oscillations of the atoms diminish the intensity of the Bragg peaks. The temporal information of this intensity change can then be studied from the evolution of MSD values. Figure 38 demonstrates this first step of fitting in a 1.5 nm thick bismuth film.

Out-of-plane MSD is computed by :

$$\Delta < u_{\perp}^2 > (\Delta t) = -log(\frac{I_{main}(\Delta t)}{I_{main,0}})/Q^2 \tag{24}$$

where $I_{main,0}$ is the intensity at negative pump delays, $I_{main}(\Delta t)$ is the intensity at a time delay and Q is the amplitude of the scattering vector. In our experiment, for reflection geometry, the scattering vector is double the the wave vector of the electron before scattering.
This is then modeled by;

$$\Delta < u_{\perp}^2 > (\Delta t) = a(1 - exp(-((t-c)/\tau_+)))\,(exp(-(t-c)/\tau_-))\,(t > c) \tag{25}$$

From this procedure, we find the fitting parameters with which we fit the intensity in each ring. τ_+ is the time constant that measures the decay of MSD, τ_- is the time constant that measures the increase of MSD and a is the amplitude associated with it.
We now fit the intensity in each ring which includes all the different contributions of rings.

$$\begin{aligned} I_q(\Delta t) = A_{ph}(1 - exp(-(t-c)/\tau_{rise}))(exp(-(t-c)/\tau_{cool}) + z) + \\ A_{bragg} exp(-62.93a(1 - exp(-((t-c)/\tau_+)))\,(exp(-(t-c)/\tau_-))\,(t > c)) + r \end{aligned} \tag{26}$$

where A_{ph}, A_{bragg} is the fitting parameter for the amplitude of the phonon contribution and Bragg contribution, respectively. The fit perfectly describes the data. (Figure 39) . Therefore, we obtain rise times in all the rings as given in Figure 36. As we move towards the zone boundary, it is evident that the contribution from the main lattice peak decreases, confirming the fit model used. Rise values were found to be similar in all the rings and showed no significant trends.

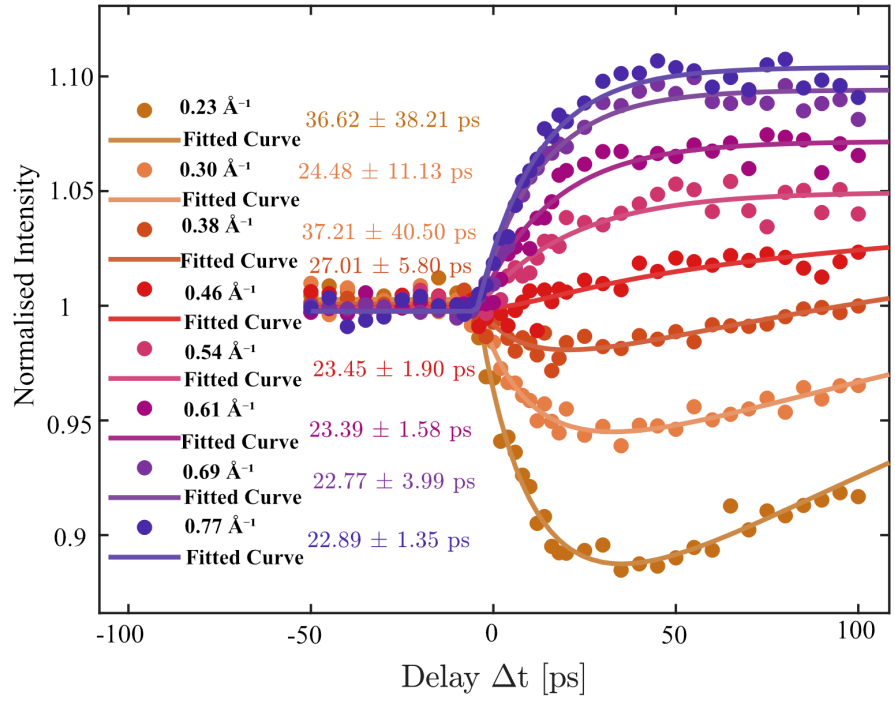

(a)

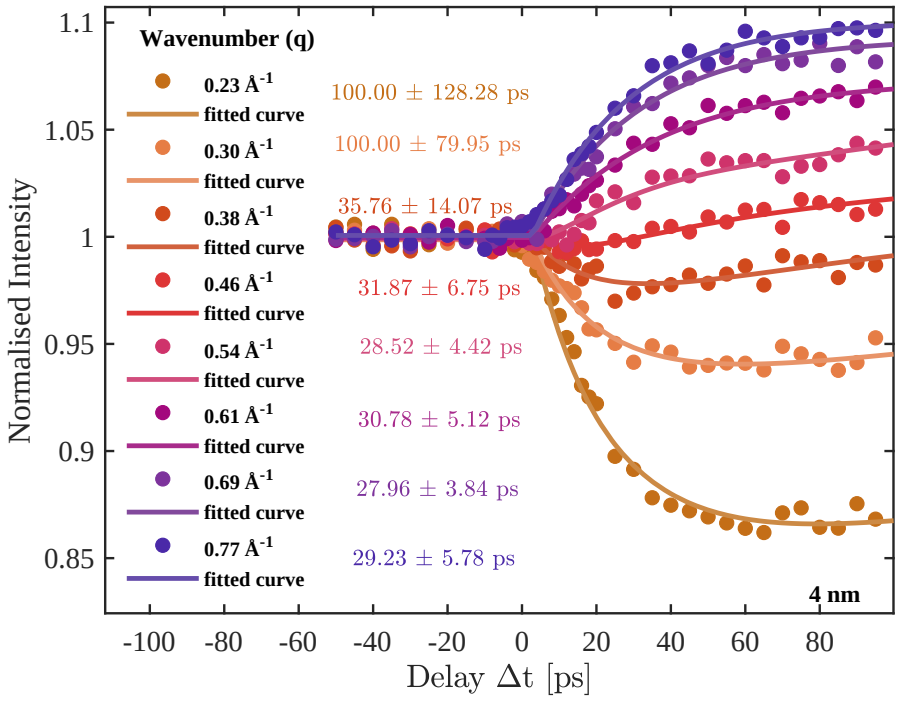

(b)

Figure 39: (a) Temporal evolution of the normalized mean intensity, fitted with equation (25) for (a) 1.5 nm bismuth film and (b) 4 nm bismuth film.

Discussion

Figure 40 and Figure 41 shows the variation of τ_{rise} and A_{ph} at different momenta for 1.5 nm and 4 nm thick bismuth films.

Unlike predicted by Hanisch-Blicharski et al. [8], a dependence of momentum-resolved rise-times for different thicknesses was not observed. Since the critical angle for total internal reflection is very small (7.3° up to 19.7°) [8], any contribution from the expected phenomenon should be observed close to the region near the Bragg spots. In our results, we find it difficult to disentangle the information from this because of several reasons like charging effects and broad Bragg spots. Our results rather indicate that there is no difference in contribution from different phonons (See Figure 42). This uniform temporal evolution indicates that all phonons behave similarly.

This study thus emphasizes the need for further investigation into the underlying properties. The distortions and possible charging effects can be a cause for not observing the expected. Increasing the integration time may render the observation of small differences possible if they exist at all. Also, taking a silicon substrate with higher conductivity can be a possible solution to reduce the charging effects.

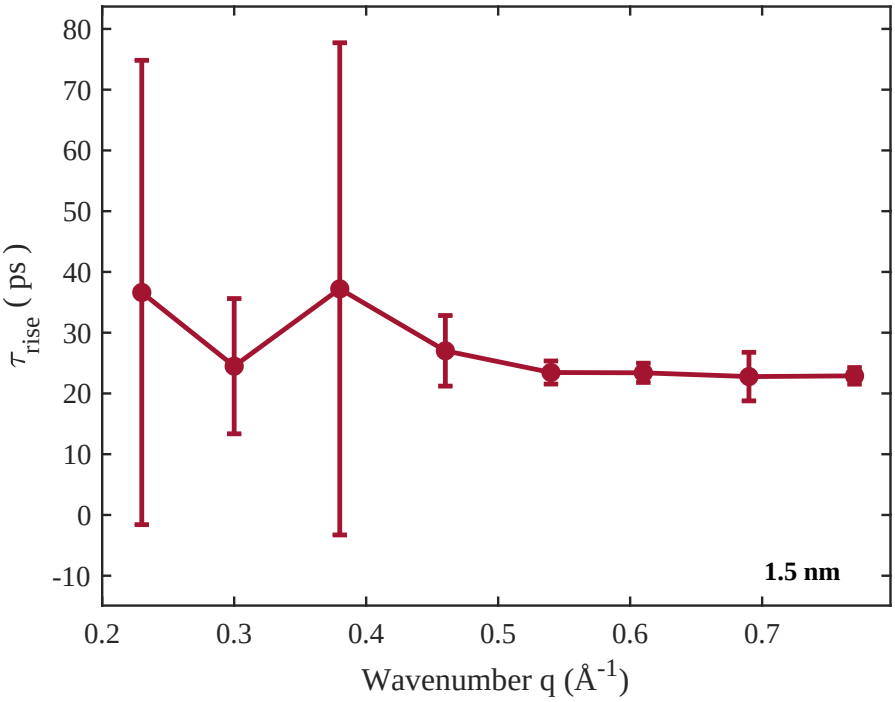

(a)

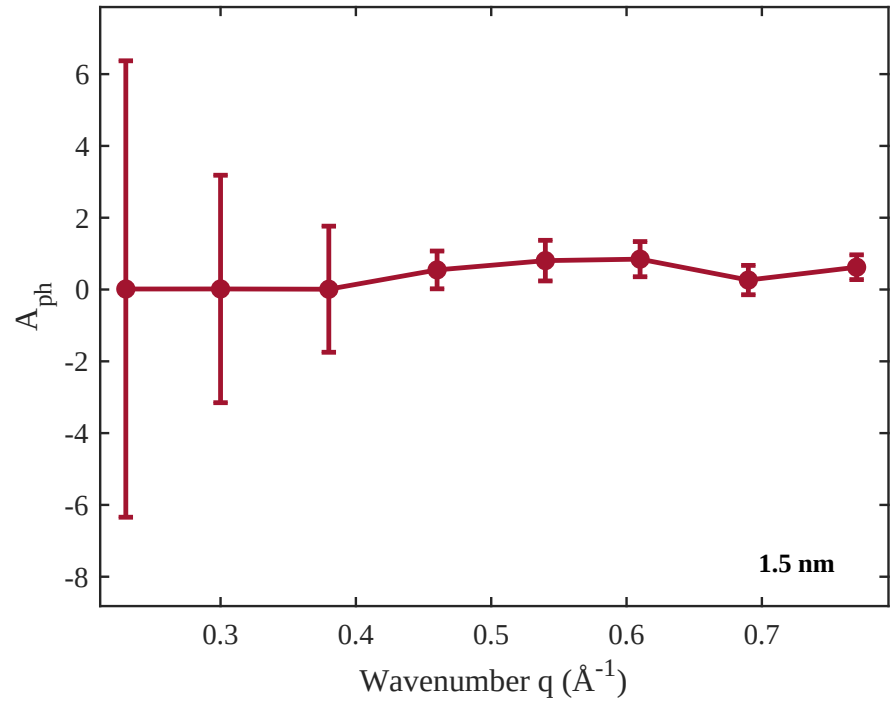

(b)

Figure 40: 1.5 nm bismuth film (a) Rise time plotted over wavenumber q. (b) A_{ph} plotted over wavenumber q.

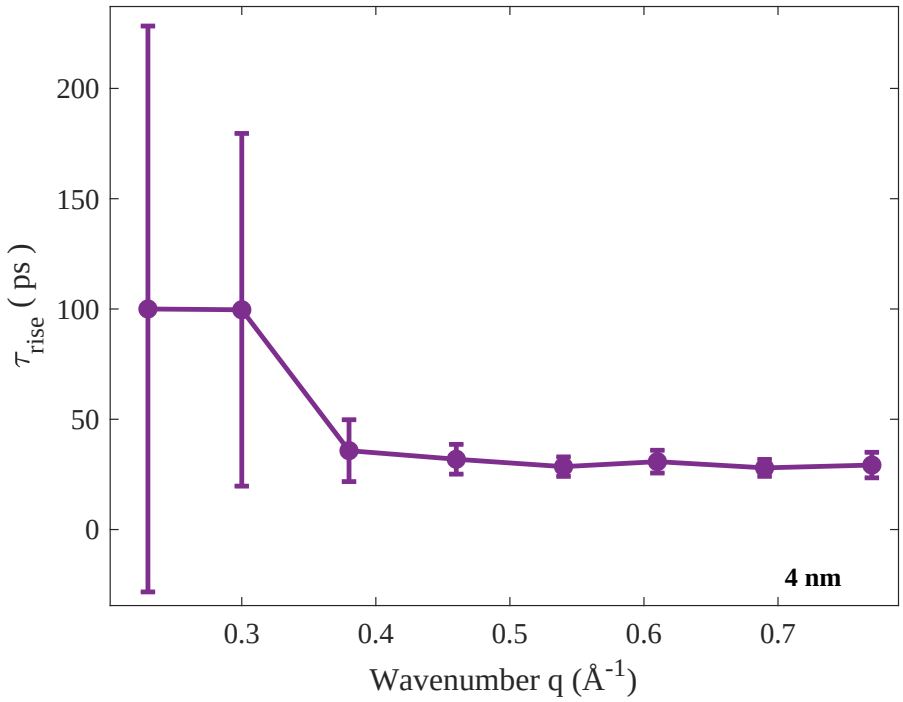

(a)

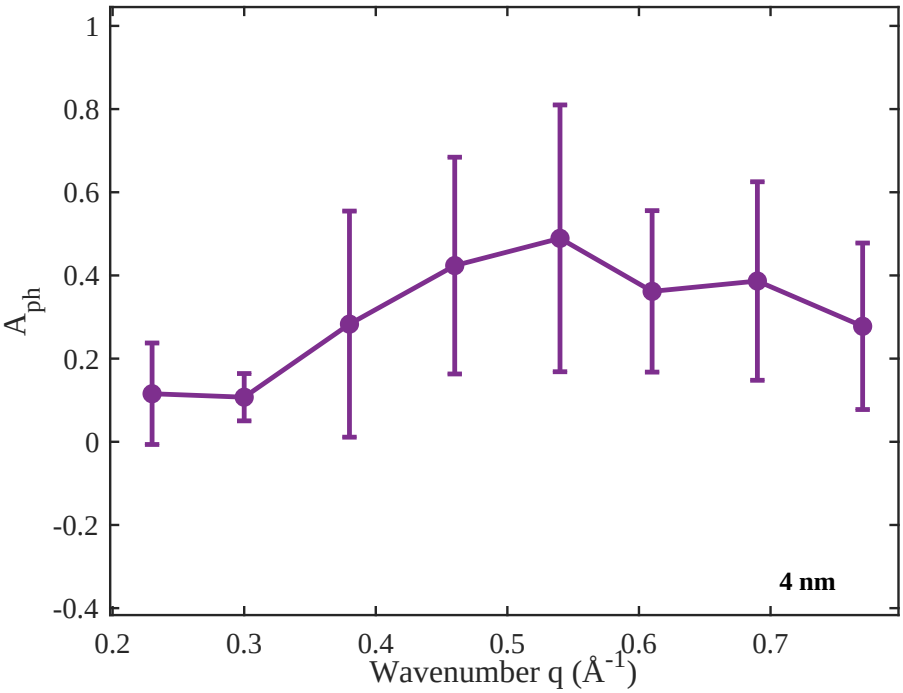

(b)

Figure 41: 4 nm bismuth film (a) Rise time plotted over wavenumber q. (b) A_{ph} plotted over wavenumber q.

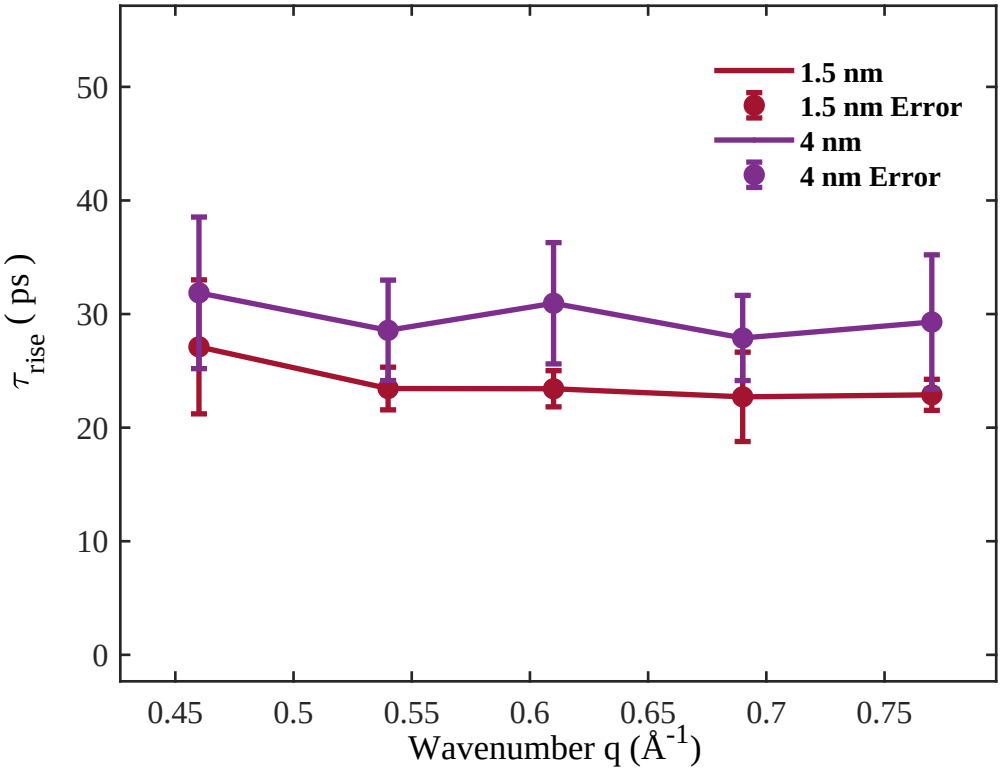

Figure 42: Rise time plotted over wavenumber q for 1.5 nm and 4 nm film.

4 Conclusion

In this thesis, ultrafast dynamics of bismuth films on Si(001) were studied using Ultrafast Low Energy Electron Diffraction (ULEED). Owing to its high temporal resolution and surface sensitivity, ULEED is a powerful tool for understanding the photoinduced structural response and phonon dynamics in bismuth films when subjected to femtosecond laser excitation.

Key parameters like rise time and cooling time constants were determined using a suitable fitting procedure. Their dependence on incident fluence and film thickness was systematically analyzed to understand the underlying mechanisms.

Our results show a decrease in rise times with increasing fluence, consistent with the inverse dependence on maximum temperature reported by Brand et al. However, this trend was not clearly observed in another set of measurements, likely due to reduced variation in rise times at higher temperatures. The cooling time was, however, found to be independent of the applied fluence. Our study reveals a deviation from the linear dependence of cooling time constant on film thickness below 3 nm, differing from previous reports that observe this deviation below 6 nm. The discrepancy may be attributed to differences in thickness calibration, deposition rates etc.

We also analyzed the diffuse background in the vicinity of Bragg spots to study momentum-resolved dynamics in the phonon population due to the Debye-Waller effect. Our experiments did not show the expected dependence of momentum-resolved rise times on the wavevector for different thicknesses, contrary to predictions by Hanisch-Blicharski et al. This absence suggests a uniform temporal evolution of phonons, potentially due to distortions, charging effects, and broad Bragg spots obscuring the expected contributions. Conducting experiments with silicon of higher conductivity could be a crucial next step in reducing charging effects enabling us to observe the phonon dynamics more accurately. This study paves the way for more precise investigations that could further unravel the fundamental mechanisms governing the thermal transport of ultrathin bismuth films.

References

1. Sunko, V. & Sunko, V. *Angle Resolved Photoemission* (Springer, 2019).
2. VanHove, M. A., Weinberg, W. H. & Chan, C.-M. *Low-energy electron diffraction: experiment, theory and surface structure determination* (Springer Science & Business Media, 2012).
3. Hunklinger, S. *Festkörperphysik 2. A.* (Oldenbourg Wissenschaftsverlag GmbH, 2009).
4. Zuo, J. M. & Spence, J. C. *Advanced transmission electron microscopy* (Springer, 2017).
5. Xu, R. & Chiang, T. C. Determination of phonon dispersion relations by x-ray thermal diffuse scattering. *Zeitschrift für Kristallographie-Crystalline Materials* **220,** 1009–1016 (2005).
6. Kurtz, F., Dauwe, T. N., Yalunin, S. V., Storeck, G., Horstmann, J. G., Böckmann, H. & Ropers, C. Non-thermal phonon dynamics and a quenched exciton condensate probed by surface-sensitive electron diffraction. *Nature Materials,* 1–8 (2024).
7. Stoner, R. & Maris, H. Kapitza conductance and heat flow between solids at temperatures from 50 to 300 K. *Physical Review B* **48,** 16373 (1993).
8. Hanisch-Blicharski, A., Tinnemann, V., Wall, S., Thiemann, F., Groven, T., Fortmann, J., Tajik, M., Brand, C., Frost, B.-O., von Hoegen, A., *et al.* Violation of Boltzmann equipartition theorem in angular phonon phase space slows down nanoscale heat transfer in ultrathin heterofilms. *Nano Letters* **21,** 7145–7151 (2021).
9. Gulde, M., Schweda, S., Storeck, G., Maiti, M., Yu, H. K., Wodtke, A. M., Schäfer, S. & Ropers, C. Ultrafast low-energy electron diffraction in transmission resolves polymer/graphene superstructure dynamics. *Science* **345,** 200–204 (2014).
10. Horstmann, J. G. *Ultrafast Probing and Coherent Vibrational Control of a Surface Structural Phase Transition* PhD thesis (Dissertation, Göttingen, Georg-August Universität, 2021, 2021).

11. Storeck, G., Vogelgesang, S., Sivis, M., Schäfer, S. & Ropers, C. Nanotip-based photoelectron microgun for ultrafast LEED. *Structural Dynamics* **4** (2017).

12. Hardie, D. & Jack, K. Crystal structures of silicon nitride. *Nature* **180,** 332–333 (1957).

13. Arblaster, J. W. *Selected values of the crystallographic properties of elements* (ASM International, 2018).

14. Martienssen, W. & Warlimont, H. *Springer handbook of condensed matter and materials data* (Springer Science & Business Media, 2006).

15. Pendry, J. B. in *Interaction of Atoms and Molecules with Solid Surfaces* 201–211 (Springer, 1974).

16. Ramstad, A., Brocks, G. & Kelly, P. Theoretical study of the Si (100) surface reconstruction. *Physical Review B* **51,** 14504 (1995).

17. Eastman, D. E. Geometrical and electronic structure of Si (001) and Si (111) surfaces: A status report. *Journal of Vacuum Science and Technology* **17,** 492–500 (1980).

18. Zandvliet, H. J. Energetics of si (001). *Reviews of Modern Physics* **72,** 593 (2000).

19. Schlier, R. & Farnsworth, H. Structure and adsorption characteristics of clean surfaces of germanium and silicon. *The Journal of Chemical Physics* **30,** 917–926 (1959).

20. Duke, C. B. Semiconductor surface reconstruction: The structural chemistry of two-dimensional surface compounds. *Chemical reviews* **96,** 1237–1260 (1996).

21. Enta, Y., Suzuki, S. & Kono, S. Angle-resolved-photoemission study of the electronic structure of the Si (001) c (4$\times$ 2) surface. *Physical review letters* **65,** 2704 (1990).

22. Jnawali, G., Hattab, H., Krenzer, B. & Horn von Hoegen, M. Lattice accommodation of epitaxial Bi (111) films on Si (001) studied with SPA-LEED and AFM. *Physical Review B—Condensed Matter and Materials Physics* **74,** 195340 (2006).

23. Meyer, D., Jnawali, G., Hattab, H. & Horn-von Hoegen, M. Rapid onset of strain relief by massive generation of misfit dislocations in Bi (111)/Si (001) heteroepitaxy. *Applied Physics Letters* **114** (2019).

24. Mönig, H., Sun, J., Koroteev, Y. M., Bihlmayer, G., Wells, J., Chulkov, E. V., Pohl, K. & Hofmann, P. Structure of the (111) surface of bismuth: LEED analysis and first-principles calculations. *Physical Review B—Condensed Matter and Materials Physics* **72,** 085410 (2005).

25. Hattab, H., Zubkov, E., Bernhart, A., Jnawali, G., Bobisch, C., Krenzer, B., Acet, M., Möller, R. & Horn-von Hoegen, M. Epitaxial Bi (111) films on Si (001): Strain state, surface morphology, and defect structure. *Thin Solid Films* **516,** 8227–8231 (2008).

26. Shirasawa, T., Mizuno, S. & Tochihara, H. Electron-beam-induced disordering of the Si (001)-c (4× 2) surface structure. *Physical review letters* **94,** 195502 (2005).

27. Kumari, L., Lin, S.-J., Lin, J.-H., Ma, Y.-R., Lee, P.-C. & Liou, Y. Effects of deposition temperature and thickness on the structural properties of thermal evaporated bismuth thin films. *Applied Surface Science* **253,** 5931–5938 (2007).

28. Bobisch, C., Bannani, A., Matena, M. & Möller, R. Ultrathin Bi films on Si (100). *Nanotechnology* **18,** 055606 (2007).

29. Jnawali, G. Growth, morphology, and conductivity in semimetallic/metallic films on Si (001) (2009).

30. Brand, C., Tinnemann, V., Hanisch-Blicharski, A., Tajik, M., Fortmann, J., Kaßen, A., Thiemann, F. & Hoegen, M. Non-Equilibrium Pathways for Excitation of Bulk and Surface Phonons through Anharmonic Coupling. *arXiv preprint arXiv:2310.15740* (2023).

31. Hanisch, A., Krenzer, B., Pelka, T., Möllenbeck, S. & Horn-von Hoegen, M. Thermal response of epitaxial thin Bi films on Si (001) upon femtosecond laser excitation studied by ultrafast electron diffraction. *Physical Review B—Condensed Matter and Materials Physics* **77,** 125410 (2008).

32. Chatelain, R. P., Morrison, V., Godbout, C., van der Geer, B., de Loos, M. & Siwick, B. J. Space-charge effects in ultrafast electron diffraction patterns from single crystals. *Ultramicroscopy* **116,** 86–94 (2012).

33. Wu, Y.-J., Fang, L. & Xu, Y. Predicting interfacial thermal resistance by machine learning. *npj Computational Materials* **5,** 56 (2019).

34. René de Cotret, L. P., Pöhls, J.-H., Stern, M. J., Otto, M. R., Sutton, M. & Siwick, B. J. Time-and momentum-resolved phonon population dynamics with ultrafast electron diffuse scattering. *Physical Review B* **100,** 214115 (2019).

35. Stern, M. J., René de Cotret, L. P., Otto, M. R., Chatelain, R. P., Boisvert, J.-P., Sutton, M. & Siwick, B. J. Mapping momentum-dependent electron-phonon coupling and nonequilibrium phonon dynamics with ultrafast electron diffuse scattering. *Physical Review B* **97,** 165416 (2018).

36. Waldecker, L., Bertoni, R., Hübener, H., Brumme, T., Vasileiadis, T., Zahn, D., Rubio, A. & Ernstorfer, R. Momentum-resolved view of electron-phonon coupling in multilayer WSe 2. *Physical Review Letters* **119,** 036803 (2017).